Evaluation of the quality of a UAV-based eddy covariance system for measurements of wind **field** and turbulent flux

Yibo Sun[1,2,3], Shaomin Liu[4], Xinwen Lin[5], Ziwei Xu[4], Bing Geng[6], Bo Liu[1,2,3], Shengnan Ji[1,2,3], Junping Jing[7], Zhiping Zhu[8,9], Bilige Sude[1,2,3], Zhanjun Quan[1,2,3]

[1]State Key Laboratory of Environmental Criteria and Risk Assessment, Chinese Research Academy of Environmental Sciences, Beijing 100012, China.
[2]Institute of Ecology, Chinese Research Academy of Environmental Sciences, Beijing 100012, China.
[3]State Environmental Protection Key Laboratory of Ecological Regional Processes and Functions Assessment, Beijing 100012, China.
[4]State Key Laboratory of Earth Surface Processes and Resource Ecology, Faculty of Geographical Science, Beijing Normal University, Beijing 100875, China.
[5]Collage of Geography and Environment Science, Zhejiang Normal University, Zhejiang 321004, China.
[6]Beijing Academy of Social Sciences, Beijing 100101, ~~BeijingChina~~China.
[7]National Ocean Technology Center, Tianjin 300112, China.
[8]Kunming General Survey of Natural Resources Center, China Geological Survey, Kunming 650111, China.
[9]Technology Innovation Center for Natural Ecosystem Carbon Sink, Ministry of Natural Resources, Kunming 650100, China.

Correspondence to: Yibo Sun (sun.yibo@ craes.org.cn) and Shaoming Liu (smliu@bnu.edu.cn)

Abstract. Instrumentation packages of eddy covariance (EC) have been developed for a small unmanned aerial vehicle (UAV) to measure the turbulent fluxes of latent heat (LE), sensible heat (H), and CO_2 ~~(Fc)~~(Fc) in the atmospheric boundary layer. This study evaluates the measurement performance of this UAV-based EC system. First, the precision (1σ) of geo-referenced wind measurement was estimated at 0.07 m s^{-1}. Then, the effect of calibration parameter and aerodynamic characteristics of the UAV on the quality of the measured wind was examined by conducting a set of calibration flights. The results shown that the calibration improved the quality of measured wind field, and the influence of upwash and leverage effect can be ignored in the wind measurement. Third, for the measurement of turbulent fluxes, the measurement error caused by instrumental noise was estimated at 0.03 µmol m^{-2} s^{-1} for Fc, 0.02 W m^{-2} for H, and 0.08 W m^{-2} for LE. Fourth, ~~the precision (1σ) of the measurements was estimated at 0.04 m s^{-1} for wind velocity, 0.08 µmol m^{-2} s for Fc, 1.61 W m^{-2} for H, 0.15 W m^{-2} for LE, and 0.02 m s^{-1} for friction velocity ($u*$). Second, the effect of calibration parameter and aerodynamic characteristics of the UAV on the quality of the measured wind was examined by conducting a set of calibration flights. The results shown that the calibration improved the quality of measured wind field, and the influence of upwash and leverage effect can be ignored in the wind measurement. Third,~~ data from the standard operational flights are used to assess the influence of resonance on the measurements and to test the sensitivity of the measurement under the variation ($\pm30\%$) of the calibration parameters around their optimum values. ~~of the system by adding an error of $\pm30\%$ to their calibrated value.~~ Results shown that the effect of resonance mainly affect the measurement of CO_2 ($\sim5\%$). The pitch offset angle (ε_θ) significantly affected the measure~~ment of~~d vertical wind ($\sim30\%$) and turbulent fluxes~~H~~ (~15~~25~~ %). The heading offset

35 angle (ε_ψ) ~~only~~ mainly affected the measurement of horizontal wind ($\sim15\%$), and other calibration parameters had no

36 significant effect on the measurements. The results lend confidence to use the UAV-based EC system, and suggest future

37 directions for optimization and development of the next generation system.

1 Introduction

39 In environmental, hydrological and climate change sciences, the measurement of surface fluxes at the regional scale (level of

40 several to tens of kilometers~~kilometers level~~) has attracted great interest despite often being considered a gordian knot

41 (Mayer et al., 2022; Chandra et al., 2022). Process-based or remote sensing (RS)-based models are often used to estimate

42 land surface fluxes of matter and energy at continental to global scales with typical spatial resolution from 1-10 km (Hu and

43 Jia, 2015; Mohan et al., 2020; Liu et al., 1999). However, observational data, especially at similar scales to models'

44 estimates, ~~are~~ is often lacking, which presents a significant challenge for the validation and evaluation of the surface flux

45 products from these models' estimates (Li et al., 2018; Li et al., 2017). On the ground, in the past decades, extensive ~~ground~~

46 eddy-covariance (EC) flux sites with their composed networks and optical-microwave scintillometer (OMS) sites have been

47 built to provide temporally continuous monitoring of surface flux~~es~~ at local (hundreds of meters around the measurement site

48 of ground EC) and path (a distance of a few hundred meters to near 10 kilometers between transmitter and receiver terminal

49 of OMS) scales (Yang et al., 2017; Liu et al., 2018; Zhang et al., 2021; Zheng et al., 2023). Generally speaking, ~~F~~flux~~es~~ from

50 ground measurements need to be scaled up to kilometers-scale to provide comparable spatial surface "relative-truth" flux

51 data for the process- or RS-based models at larger spatial scales (Liu et al., 2016). However, the spatial density of these flux

52 measurements sites is still low compared to the ~~complex variability~~heterogeneity of surface fluxes, which means that major

53 scaling bias may exist in the upscaled flux data (Wang et al., 2016; Li et al., 2021). Therefore, regional-scaled flux

54 measurement techniques need to ~~are needed to~~ be developed to complement the ground- and models-based approaches

55 (Vellinga et al., 2010).

56 ~~The a~~Aircraft-based EC flux measurement method, which has been developed for turbulence measurements for more than

57 40 years (Lenschow et al., 1980; Desjardins et al., 1982), is considered as the optimum method to measure turbulent flux at

58 regional scale (several hundred square kilometers), thus bridging the scale gap between ground and model-derived methods

59 (Gioli et al., 2004; Garman et al., 2006). To date, several types of aircrafts, including manned or unmanned fixed-wing

60 aircrafts, delta-wing aircrafts, and helicopters, have been used for measurements of turbulent flux by equipping them with

61 the EC sensors to measure three-dimensional (3D) wind, air temperature, and gas concentrations at ~~high~~ a frequency of 50

62 Hz (Gioli et al., 2006; Metzger et al., 2012; Thomas et al., 2012; Bange and Roth, 1999). Among them, fixed-wing aircrafts

63 and delta-wing aircrafts are better airborne platforms for EC measurements compared to helicopters due to their tightly

64 coupled structure with the wind sensor and because their flow distortion around the fuselage can be more easily avoided or

65 modeled (Prudden et al., 2018; Garman et al., 2008). A wide range of manned aircrafts has been developed to measure

66 turbulent flux, including single-engine light aircrafts (e.g., Sky Arrow 650, Long-EC, WSMA) (Gioli et al., 2006; Crawford

67 and Dobosy, 1992; Metzger et al., 2012), twin-engine aircrafts (e.g., Twin Otter, NASA CARAFE) (Desjardins et al., 2016;

68 Wolfe et al., 2018) and larger quad-engine utility aircrafts (e.g., NOAA WP-3D) (Khelif et al., 1999). These airborne flux

69 measurements, in combination with ground measurements, provide an excellent opportunity to produce regional-scaled,

70 spatio-temporal continuous surface flux datasets that can improve our understanding of the ~~interactive~~ processes ~~between the~~

71 ~~land surface and the atmosphere~~of land-atmosphere interactions in regional and global change (Chen et al., 1999; Liu et al.,

72 1999; Prueger et al., 2005). However, manned aircrafts are expensive to operate and maintain. Aviation safety and

73 operational regulations require that manned aircrafts must fly above a minimum altitude (400 m above the highest elevation

74 within 25 km on each side of the center line of the air route) and must avoid hazardous conditions such as icing or severe

75 turbulence (Elston et al., 2015). The flow distortion induced by the aircraft itself (from the wings, fuselage, and the

76 propellers) complicates the wind vector measurement from aircraft platform, which means that sophisticated correction

77 procedures should be applied to compensate for the flow distortion effects (Elston et al., 2015; Williams and Marcotte, 2000;

78 Drüe and Heinemann, 2013).

79 In recent years, interest~~ing~~ in unmanned aerial vehicle (UAV) ~~fixed-wing~~ platforms for atmospheric studies ~~has~~have been

80 fast growing, especially because of their lower construction, operation, and maintenance costs compared with manned

81 platforms. High-performance fixed-wing UAVs offer a high payload capacity (5-10 kg) and similar endurance (2-3 h) and

82 operating altitude (up to 3500 m above the sea level) to manned aircrafts, but with much less turbulence disturbance due to

83 their small fuselage size (Reineman et al., 2013). More importantly, the advancements in small, fast, and powerful sensors

84 and microprocessors make it possible to use of UAVs for comprehensive atmospheric measurements (Sun et al., 2021a).

85 Several types of UAVs with different turbulence measurement objectives have been developed and deployed, ranging from

86 small payload capacity (e.g., 140 g SUMO) to medium (e.g., 1.5 kg M^2AV, 1.0 kg MASC) and large (e.g., 6.8 kg Manta, 5.6

87 kg ScanEagle) (Reuder et al., 2016; Båserud et al., 2016; Van Den Kroonenberg et al., 2012; Reineman et al., 2013). A

88 comprehensive overview of the use of these UAVs for turbulence sampling can be found in Elston et al. (2015) and Sun et al.

89 (2021a). For turbulence measurements, the UAVs were equipped with a commercial or custom multi-hole (5- or 9-hole)

90 probe paired with an integrated navigation system (INS) to obtain the wind vector. Small and medium UAVs typically could

91 only measure fast 3D wind vector and air temperature fluctuations for measurements of momentum and sensible heat flux,

92 whereas, large UAVs were equipped with more types (e.g., radiation, ~~image~~optics, or gas concentration) and more accurate

93 sensors for measurement of a larger range of meteorological properties including sensible and latent heat fluxes, CO_2 flux,

94 radiation fluxes as well as surface properties (Reineman et al., 2013; Sun et al., 2021a). UAVs equipped with scientific

95 instruments can be deployed in a variety of application environments and conditions. UAVs offer distinct advantages over

96 manned aircraft in their ability to safely perform measurements and greatly reduce operational costs especially in low-

97 altitude conditions (below 100 m above the ground level), which are optimal for measuring turbulent flux (Witte et al., 2017).

98 Anderson and Gaston (2013) predict that UAVs will revolutionize the spatial data collection in ecology and meteorology.

99 ~~The~~ EC method is a well-developed technology for directly measuring vertical turbulent flux (flux of sensible heat, ~~matter~~

100 latent heat and ~~momentum~~CO_2) within the atmospheric boundary layers (ABL) (Peltola et al., 2021). It requires accurate time

101 (for ground tower) or spatial (for mobile platform) series of both the transported scalar quantity and the transporting

102 turbulent wind. Each should be measured at sufficient frequency to resolve the flux contribution from small eddies (Vellinga

103 et al., 2013). The measurement of the geo-referenced 3D wind vector, which is the prerequisite for EC measurements, is

104 challenging for airborne platform. Airborne measurement of geo-referenced 3D wind is the vector sum between the aircraft

105 velocity relative to the earth (inertial velocity) and the velocity relative to the air (relative wind vector, or true airspeed).

106 Therefore, accurate measurements of the relative wind as well as the motion and attitude of the platform are essential to

107 accurately measure the geo-referenced wind vector and turbulent flux (Metzger et al., 2011). Garman et al. (2006) estimated

108 the measurement 1σ precision (1σ) of the vertical wind measurements of a commercial 9-hole turbulence probe (known as

109 "Best Air Turbulence Probe", often abbreviated as the "BAT Probe") to be 0.03 m s^{-1} by combining the precision of the BAT

110 Probe and the integrated navigation device. The BAT Probe is widely used on manned fixed-wing aircrafts, such as Sky

111 Arrow 650 ERA (Environmental research aircraft), Beechcraft Duchess, and Diamond DA42, for turbulent flux

112 measurement (Gioli et al., 2006; Garman et al., 2008; Sayres et al., 2017). A light delta-wing EC flux measurement aircraft

113 developed by Metzger et al. (2011) reported a 1σ precision of wind measurement of 0.09 m s^{-1} for horizontal wind and 0.04

114 m s^{-1} for vertical wind using a specially customized five-hole probe (5HP). On this basis, in combination with a commercial

115 infrared gas analyzer, the 1σ precision of flux measurement was 0.003 m s^{-1} for friction velocity, 0.9 W m^{-2} for sensible

116 heat flux, and 0.5 W m^{-2} for latent heat flux. The smallest resolvable magnitudes for the wind velocity and turbulent flux

117 were estimated from these values by assuming a signal-to-noise ratio of 5:1 (Metzger et al., 2012). The EC flux measurement

118 from a UAV platform can now be achieved with a similar reliability to a manned platform. The Manta and ScanEagle UAV-

119 based EC measurements developed by Reineman et al. (2013) achieved precise wind measurements (0.05 m s^{-1} for horizontal

120 and 0.02 m s^{-1} for vertical wind) using a custom nine-hole probe and a commercial high precision integrated navigation

121 system (INS) integrated navigation system (INS), at a lower price and lighter weight than the commercial BAT probe.

122 However, the onboard instrument packages for Manta and ScanEagle UAV are independent of each other in their

123 measurements of turbulent and radiation flux, and the CO_2 flux measurement is lacking.

124 Inspired by these studies, Sun et al. (2021a) used a high-performance fuel-powered vertical take-off and landing (VTOL),

125 fixed-wing platform to integrate the scientific payloads for EC and radiation measurements to obtain a comprehensive

126 measurement of turbulent and radiation flux using an UAV. This UAV-based EC system measured turbulent fluxes

127 including of sensible heat, latent heat, and CO_2, as well as radiation including net radiation and upward- and downward-

128 looking photosynthetically active radiation (PAR). This system was successfully tested in the Inner Mongolia of China and

129 applied to measure the regional sensible and latent heat fluxes in the Yancheng coastal wetland in Jiangsu, China (Sun et al.,

130 2021a; 2021b). During these field studies, the UAV-based EC measurements achieved a near consistent observational result

131 compared with ground EC measurements (Sun et al., 2021b). However, some shortcomings in the developed UAV-based EC

132 system were also identified. In particular, the noise effects from the engine and propeller were not fully isolated, resulting in

133 high frequency noise in the measured scalars (air temperature, H_2O, and CO_2 concentration). This UAV-based EC system is

134 being continuously improved (in Section 2.1) based on previous field measurements. However, there is no quantitative

135 evaluation of the measurement ~~capability~~precision of the wind field and turbulent flux ~~or~~as well as of the influence of the

136 resonance noise from the UAV ~~based EC measurement system~~ operation yet. Previous work using ground EC ~~measurements~~

137 as a benchmark to assess the measurement performance of the UAV-based EC system has been disputed, due to difference in

138 EC sensors, platforms, measurement height, and source areas (i.e., footprint), as well as the influence of surface

139 heterogeneity, flux divergence, inversion layer and the stochastic nature of turbulence (Sun et al., 2021b; Wolfe et al., 2018;

140 Hannun et al., 2020).

141   This study attempts to ~~quantitatively~~ evaluate the performance of ~~a~~ the UAV-based EC system developed by Sun et al.

142 (2021a) in the measurement of wind field and turbulent flux~~es~~. For these purposes, data from two field measurement

143 campaigns, including a set of calibration flights and some standard operation flights, were used in this study. First, the

144 current study investigated~~s~~ the quality of the measurement of geo-referenced wind vector including measurement error (1σ)

145 and the improvements for wind measurement after system calibration. Second, using the measured data from standard

146 operation flights, flux measurement error related to instrumental noise was estimated with a method proposed by Billesbach

147 (2011). Errors propagated through the correction terms [i.e., Webb-Pearman-Leuning (WPL) correction for latent heat and

148 CO_2 flux] were also included in our analysis (Webb et al., 1980; Kowalski et al., 2021). Then, the impacts of resonance noise

149 on the measured scalar variance and the flux covariance were also estimated by comparing the real (co)spectra curve with the

150 theoretical reference curve from Massman and Clement (2005). Lastly, the sensitivity of the measured geo-referenced wind

151 vector and turbulent flux to the errors in the calibration parameters (determined by the calibration flight) were assessed by

152 adding an error of ±30 % to their optimum calibration value.

153   ~~the 1σ measurement error of the geo-referenced wind vector and turbulent flux by propagating the error of each EC sensor~~

154 ~~along the data process procedure. Then, a set of calibration flights were conducted to assess how the calibration parameters~~

155 ~~and aerodynamic characteristics of the UAV affect the quality of the wind measurement. The effects of resonance noise on~~

156 ~~the measured scalar variance and the fluxes were also estimated by comparing the real (co)spectra curve with the theoretical~~

157 ~~reference curve from Massman and Clement (2005). Lastly, the sensitivity of the measured geo-referenced wind vector and~~

158 ~~turbulent flux to the calibration parameters (determined by the calibration flight) were assessed by adding an error of ±30 %~~

159 ~~to their optimum calibration values.~~

160 **2 Materials and Methods**

161 **2.1 The UAV-based EC system**

162 The UAV platform used for EC measurement is a high-performance, fuel-powered VTOL, fixed-wing UAV, which has

163 minimal requirements for the takeoff location and offers a high payload capacity of up to 10 kg. The UAV has a wing-span

164 of 3.7 m, a fuselage length of 2.85 m, and a maximum take-off weight of 60 kg. The UAV engine is mounted in a pusher

165 configuration, allowing for the turbulence probe to be installed directly on the nose of the UAV, minimizing or eliminating

166 airflow contamination due to upwash and sidewash generated by the wings (Crawford et al., 1996). Control of the UAV is

167 totally autonomous, and the pilots have the option to enable manual and semi-manual control in emergency conditions. The

168 UAV has a cruise flight speed of 28 to 31 m s^{-1} with an endurance of almost 3 h, and it has a flight ceiling of up to 3800 m

169 above the sea level. Detailed information on this UAV could be found in Sun et al. (2021a).

170 The ~~flux~~flux payloads of the UAV-based EC system include a precision-engineered 5-hole pressure probe (5HP) for

171 measurement of the true airspeed and the attack (α) and sideslip (β) angles of incoming flow relative to the UAV, a dual-

172 antenna integrated navigation system (INS) for high accuracy measurement of UAV ground speed and attitude, an open path

173 infrared gas analyzer (IRGA) for recording the atmospheric densities of CO_2 and water vapor, a fast temperature sensor for

174 measurement of the fast temperature fluctuations, and a slow-response temperature probe for providing a mean air

175 temperature reference. ~~The auxiliary payloads include a net radiometer and two photosynthetically active radiation (PAR)~~

176 ~~radiometers that look upward and downward.~~ The sample rate ~~of the flux payloads~~ is 50 Hz except for the slow-response

177 temperature probe (1 Hz), yielding a turbulence horizontal resolution of approximately 1.2 m at a cruising speed of 30 m s^{-1}.

178 The system was improved according to deficiencies identified after several field measurements with the following

179 adjustments: 1) a laser distance measurement unit was mounted for measuring the distance between the UAV and the ground

180 level, 2) the platinum resistance thermometer was replaced by a thermocouple (Omega T-type COCO-003; Ø0.075 mm) for

181 improving the resistance of the high-frequency temperature measurements to vibration noise from the engine, 3) the

182 vibration isolator structure of the IRGA was improved, and 4) the original datalogger (CR1000X, Campbell, USA) was

183 replaced with a lighter one (CR6, Campbell, USA). All the digital and analog signals from the ~~measurement~~ sensor~~s~~ modules

184 are stored and synchronized by the on-board datalogger, and the on-board scientific payloads are designed to be isolated

185 from the electronic components of the UAV to ensure that any problems occurring would not jeopardize the safety of the

186 UAV (Sun et al., 2021a).

187 In the present study, to estimate the measurement~~1σ~~ precision ~~for~~ of the ~~measured~~ geo-referenced wind and turbulent flux,

188 the sensor modules and the~~ir~~ 1σ precision of the measure~~ment~~d variables related to EC measurement were used, as presented

189 in Table 1. For the 5HP, the 1σ measurement precision was acquired from the wind tunnel test after ~~the~~ wind tunnel

190 calibration (Sun et al., 2021a).

191 **Table 1**: Summary of t~~T~~he sensor modules, measured variables, and their measurement p~~1σ p~~recision used to determine the

192 geo-referenced wind velocity and turbulent flux.

Sensor (Module, company, country)	Variables	Precision (1σ)
GNSS/INS (~~Trimble~~ BD992-INS, Trimble, USA)	Roll, Pitch, Heading	0.1º
	Horizontal velocity	0.007 m s^{-1}
	Vertical velocity	0.02 m s^{-1}
5HP (~~Simtec AG~~ ADP-55, Simtec AG, Switzerland)	Attack angle	0.02º[#]
	Sideslip angle	0.04º[#]
	True airspeed	0.05 m s^{-1}[#]

		Static pressure	1.1 hPa
		Dynamic pressure	0.003 hPa
IRGA	(~~Campbell~~ EC150, Campbell, USA)	CO_2 density	0.2 mg m^{-3}
		H_2O density	0.004 g m^{-3}
Thermistor	(~~BetaTherm~~ 100K6A1IA, Campbell, USA)	Temperature (slow)	0.2 ℃
Thermocouple	(~~Omega~~ T-type COCO-003, Omega, USA)	Temperature (fast)	0.5 ℃

193 # Results from the wind tunnel test.

2.2 Field campaign

2.2.1 In-flight calibration campaign

In order to calibrate the wind measurement component of the UAV-based EC system, ~~A~~an in-flight calibration campaign was carried out on 4 September 2022 at the Caofeidian Shoal Harbor ~~(39º2′55″ N, 118º38′48″ E)~~ in the Bohai Sea of northern China. The average water depth of this area is approximately 0-5 m, with a maximum water depth of 22 m. At low tide, a large area of the tidal flat is exposed; while at high tide, only the barrier islands are visible (Xu et al., 2021). The assumptions for calibration flight include 1) low turbulent transport condition (i.e., no disturbance), 2) a constant mean horizontal wind, and 3) mean vertical wind near zero (Drüe and Heinemann, 2013; Vellinga et al., 2013; Van Den Kroonenberg et al., 2008). This allows identical wind components for several consecutive straights in opposite or vertical flight directions. These assumptions are usually well satisfied above the ABL or under stable atmospheric conditions (Drüe and Heinemann, 2013). Over the sea surface, due to its uniform and cool surface property, the turbulence fluctuations are weaker than that over the land surface (Mathez and Smerdon, 2018), making ~~where~~ a more ideal environment to conduct calibration flight.

~~The optimum atmospheric conditions for the in-flight calibration include 1) no large turbulent transport, 2) a constant mean horizontal wind, and 3) mean vertical wind near zero (Van Den Kroonenberg et al., 2008). These conditions are easier to meet over the sea surface than land, due to the uniform nature of the sea surface. Additionally, the sea-atmosphere interaction is relatively weaker than the land-atmosphere interaction (Mathez and Smerdon, 2018).~~

The in-flight calibration campaign included three flight maneuvers, including a 'box' maneuver, 'racetrack' maneuver, and 'acceleration-deceleration' maneuver. The trajectory of the calibration flight is shown in Figure 1, with different color corresponding to different flight maneuver~~s~~. The calibration flight was executed between 7:28-7:48 a.m. (China Standard Time, CST) to coincide with the ebb tide stage. During this time, the average water depth was approximately 1.1 m, and the average flight altitude was 400 m ($\sigma =\pm$ 0.78 m) above the sea level. Considering the ~~conditions of the regional~~ uniform and cool underlying surface ~~and~~ and the stable atmospheric conditions ~~-~~in the early morning, we assume no disturbance from underlying surface was present during the calibration flight.

218

219
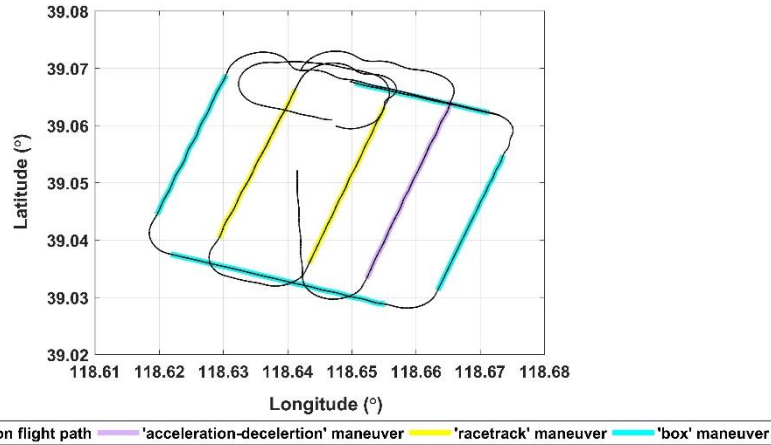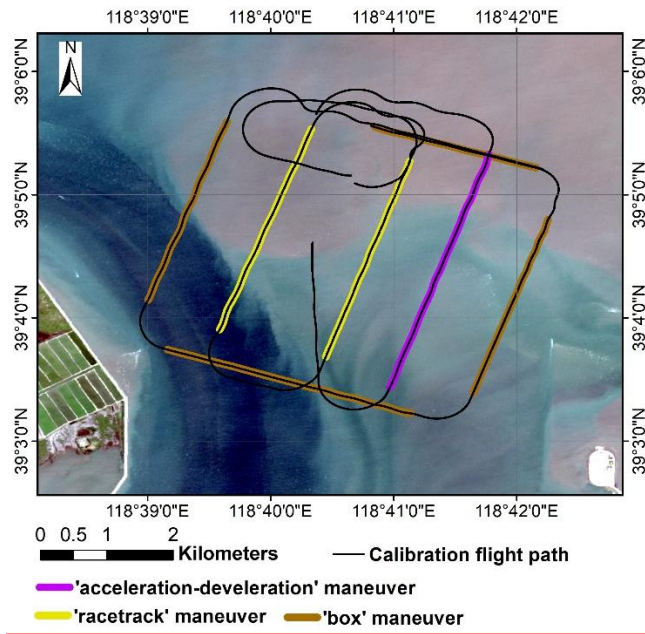
Figure 1. Flight trajectory of the calibration campaign on 4 September 2022 at the Caofeidian Shoal Harbor in the Bohai Sea of northern China. The land surface image is from Sentinel-2A satellite image with true color combination acquired on 1 September 2022.

In this study, the 'box' maneuver is used to determine the mounting misalignment angle in the heading (ϵ_ψ) and pitch (ϵ_θ) between the 5HP and the center of gravity (CG) of the UAV. The flight path is a box in which the four straight legs are flown at constant cruising speed, flight altitude, and heading for 2 minutes. The 'racetrack' maneuver is used to evaluate the quality of the calibration parameters acquired from the previous 'box' maneuver. The flight path consists of two parallel straight flight tracks connected by two 180° turns. Each straight flight section lasts 2 minutes at constant speed and flight altitude. Lastly, the 'acceleration-deceleration' maneuver is used to check the influence of lift-induced upwash from the wing to the measured attack angle by the 5HP. During this maneuver, the aircraft is kept straight and level at constant pressure

altitude. When beginning this maneuver, the aircraft accelerates to its maximum airspeed (35 m s^{-1}). Then, the airspeed reduces gradually to near its minimum airspeed (25 m s^{-1}) and back up to its maximum airspeed. The pressure-altitude of the aircraft is maintained throughout this maneuver, and the entire maneuver lasts one minute. This maneuver creates a series continuous changed pitch (θ) and attack (α) angle. A relationship between the measured incident flow attack angles (α) by the 5HP and the measured pitch angle by the INS of close to 1:1, indicates that the effect from the fuselage-induced flow distortion on the wind measurements is negligible (Garman et al., 2006).

2.2.2 Standard operation flight campaign

The reliability of the EC measurement from UAV is susceptible to several factors, mainly including instrumental noise, resonance noise, and the quality of the calibration parameter. In order to evaluate the flux measurement error related to instrumental noise, the effects of resonance on the measured scalar and to investigate the sensitivity of the measured geo-referenced wind and turbulent flux to uncertainty in the calibration parameter, Previous studies have shown that the measured scalars were affected by the vibration noise from the engine and propeller of the UAV (2021b; Sun et al., 2021a). In order to evaluate the effects of resonance on the measured scalar and to investigate the sensitivity of the measured geo-referenced wind and turbulent flux to uncertainty in the calibration parameters, we used data from 7 flights in the Dagang district (38º54′27″ N, 117º48′16″ E) in Tianjin, China between 8 and 16 August 2022. This area is located on the west coast of the Bohai Sea and is a coastal alluvial plain with altitudes between 1-3 m (Chen et al., 2017). The flight path, shown in Figure 2, includes three parallel transect lines of approximately 4 km in length each and at 1-2 km intervals. All flights occurred during the daytime, and were performed in the same trajectory at low altitude about 90 m above sea level. The flight area covered three different underlying surfaces: land, coastal zone, and water surfaces, that can represent typical flux intensity characteristics for different surface conditions.
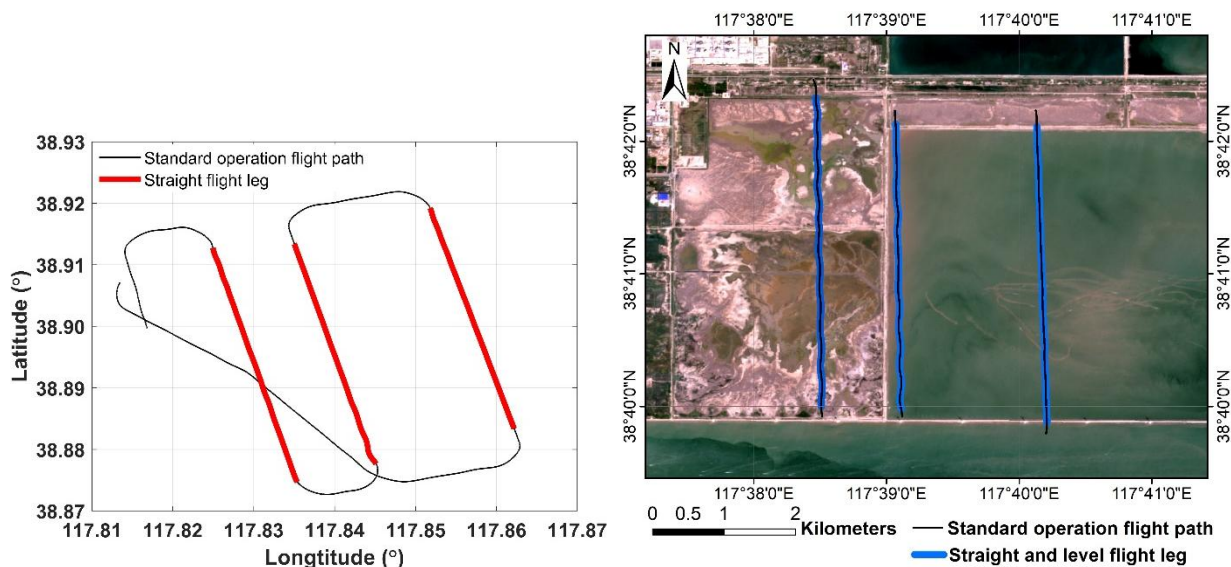
Figure 2. Flight trajectory of the standard operation flight campaign, 8-16 August 2022, at Dagang district, Tianjin, China. The land surface image is from Sentinel-2A satellite image with true color combination acquired on 27 August 2022.

During the operation flight campaign, the atmospheric stability conditions changed from stable (Monin-Obukhov stability parameter, $z/L = 1.93$) to very unstable ($z/L = -10.28$) as measured by the UAV, where z is the flight height above the ground level, L is the Obukhov length. The stable condition mostly occurred on flight path located over the sea surface, while the unstable condition mostly occurred on flight path located over the land surface. ~~The average net radiation of each transect flight line changed from -40 W m⁻² over the sea surface to 626 W m⁻² over the land surface.~~ These flight data provide various measurement conditions for us to evaluate the performance of the UAV-based EC system.

2.3 Data processing

The raw data collected with the on-board datalogger (CR6, Campbell, USA) is subsequently saved in Network Common Data Form (netCDF) format. It includes dynamic and static pressure, attack, and sideslip angle of incoming flow; slow (1 Hz) and fast (50 Hz) air temperature; mass concentration of H_2O and CO_2; as well as the full navigation data (including 3D location, ground speed, angular velocity, and attitude, etc.) of the UAV. The subsequent data processing includes three basic processing stages in order to calculate flux data from raw measured data.

In the first stage, ~~Before processing the raw data into geo-referenced wind vector and turbulent flux,~~ a moving average filter was used to detect outliers in each variable. Detected outliers were removed and replaced by values obtained by linear interpolation. Outliers tend to be rare. However, if outliers constitute more than 20 % of the data points, the corresponding flight data should be discarded. The cleaned raw data was then used to calculate the geo-referenced wind vector, (co)spectra, and turbulent fluxes.

In the second stage, geo-referenced 3D wind vector is calculated. ~~2.3.1 Wind measurements~~

The full form of the equations of motion for calculating the geo-referenced wind vector by ~~our~~ the UAV-based EC system is described in detail~~ed~~ in Supplement Part A. From the aircraft platform, geo-referenced ~~turbulent~~ wind vector is measured in two independent reference coordinate systems: the relative true airspeed ($\widehat{U}_a$) measurement in the aircraft coordinate system and the ground speed of the aircraft (U_p) in the geo-referenced coordinate system. The geo-referenced wind (U) is the vector sum of the relative true airspeed ($\widehat{U}_a$), the UAV's motion (U_p) and the tangential velocity due to the rotational motion of the aircraft ("lever arm" effect), which is described in Eq. (S2). In this stage, the acquired calibration parameters (ϵ_ψ and ϵ_θ) from the calibration flight are substituted into the Eq. (S8) to correct the mounting angle offset errors between the 5HP and the CG of the UAV. The final equations for geo-referenced wind vector calculation (Eqs. S15 to S17) revealed that the lever arm effects due to the spatial separation between the tip of the wind probe and the CG of UAV can influence the wind measurements.

The relative wind vector ($\widehat{U}_a$) measured by the aircraft is susceptible to flow distortion because the airplane must distort the flow to generate lift and thrust, and the aircraft's propellers, fuselage, and wings are the main sources of flow distortion as flow barriers (Metzger et al., 2011). For fixed-wing aircrafts, the wind probe mounted on the nose of the UAV and extended as far forward of the fuselage as possible could avoid significant influence from flow distortion from the fuselage and propellers. Nevertheless, the wind measurement is still subject to lift induced upwash due to the wings distorting the flow to generate lift and thrust. The influence of upwash decreases with linear distance from the wing and appears as an additional vertical component of airflow ahead of the wind probe (Crawford et al., 1996; Garman et al., 2008). The magnitude of upwash influence generally increases with airplane size and airspeed, typically ranging from 0.5 to 2.5 m s^{-1} as reported by the manned fixed-wing aircraft (Garman et al., 2008). Therefore, for EC measurements by manned fixed-wing aircrafts, the upwash effects must be corrected for wind measurements (Garman et al., 2008; Kalogiros and Wang, 2002). However, wind measurements using a multi-hole probe on the UAV seldom need this correction due to the fuselage size and because the airspeed is very low compared to a manned aircraft. This is considered in the equations for relative wind calculation (in Supplement) used in this study as well. The 'acceleration-deceleration' flight maneuver (Section 2.2.1) was used to assess whether the lift-induced upwash could be safety ignored by the UAV-based EC system.

The lever arm effects due to the spatial separation between the tip of the wind probe and the CG of UAV can influence the wind measurements (Eqs. S15 to S17). Typically, the separation distance (L) is small, and the influence of the lever arm effects can be ignored when the L is less than about 10 m (Lenschow, 1986). In the current UAV-based EC system, the displacements of the 5HP tip with respect to the CG of the UAV along the three axes of UAB body coordinate are: $x^b = 1.459$ m, $y^b = 0$ m, and $x^b = 0.173$ m (in Supplement Part A). Therefore, in practice, the influence of leverage effects in geo-referenced wind calculation was also ignored in this study. ; thus, the influence of leverage effects in geo-referenced wind calculation was also ignored. This was confirmed by assessing the difference in the geo-referenced wind vectors with and without the leverage effect correction term (in Section 3.1).

In the final stage, 2.3.2 Spectra and turbulent flux calculation

Unlike traditional ground-based EC measurements, those recorded on aircraft platforms are subject to several simultaneous motions, including flow distortion around the fuselage and resonance from the rotation of the engine and propeller. Spectral analysis is an effective way to assess if and to what extent the UAV's motion influences the EC measurements. For this reason, the fast Fourier transform (FFT) method was used to calculate the spectra and co-spectra of the measured turbulent variables. Before calculating the turbulence (co)spectra, condition of the raw turbulence data was performed, including a linear detrend and tapering using the Hamming window to reduce the spectral leakage (sharp edge) according to Kaimal et al. (1989).

Bbased on the EC technology and spatial averaging, the turbulent flux is calculated using the covariances of vertical wind (w) with horizontal wind components (u, v) for vertical flux of momentum (τ), with virtual potentialair temperature ($T_a\theta_v$) for sensible heat flux (H), with water vapor density (q) for latent heat flux (LE), and with CO_2 density (c) for CO_2 flux (F_c),

316 and with the necessary correction (Webb et al., 1980). The time lag due to the separation between the 5HP tip, the adjacent

317 temperature probe, and the open-path gas analysis did not need to be corrected because the time delay was less than 1 second

318 at the cruise airspeed of 30 m s^{-1} and sensor separation less than 20 cm. Only the measurement data from the straight-line

319 portion of the flight path can be used in flux calculation. Detailed calculation procedure and formulas of H, LE, and F_c used

320 by the present UAV-based EC system are provided in Supplement Part B, including spatially averaging, coordinate rotation,

321 and necessary correction (i.e., WPL correction for LE and F_c).

322 Detailed information about the EC method and airborne EC calculation can be found in other studies (Aubinet et al., 2012;

323 Vellinga et al., 2013; Gioli et al., 2006).

324 One important aspect for airborne EC measurement is the definition of a proper spatial averaging length to calculate

325 turbulent flux (Sun et al., 2018). Such spatial averaging length depends on the flying altitude, surface characteristics, and

326 atmospheric stability, and could be determined using Ogive analysis (Gioli et al., 2004; Kirby et al., 2008). In this study, the

327 objective is not to quantify the actual flux exchange between the surface and the atmosphere, but rather to assess the

328 sensitivity of the calculated turbulent flux to external parameters. Therefore, the entire measurement measured data of each

329 straight and level flight leg (each with length about 4 km) from the standard operational flight campaign was used to

330 calculate turbulent flux, regardless of the uncertainty of the flux resultsin fluxes associated with spatial averaging.

331 **2.4 Evaluation strategyscheme**

332 **2.4.1 Propagation of sensor errorsWind measurement evaluation**

333 The EC technique relies upon the precise measurement of the geo-referenced wind vector and atmospheric scalarsThe key to

334 successful aircraft EC measurements lies in the translation of accurately measured, aircraft-orientated, wind vector to geo-

335 referenced orthogonal wind vector (Thomas et al., 2012). Measured from an aircraft, dDetermining the geo-referenced wind

336 vector requires a sequence of thermodynamic and trigonometric equations, and the calculation of turbulent flux also needs a

337 series of data operations and corrections to the turbulent variables (Metzger et al., 2012). The EC data processing procedure

338 and, these equations propagate various sources of error to the measured geo-referenced wind vector and turbulent flux. To

339 estimate the measurement errors in the geo-referenced wind vector, we used the linearized Taylor series expansions of Eqs.

340 (S15) to (S17) derived by Enriquez and Friehe (1995) (in Supplement Part A) to determine the sensitivities of each of the

341 geo-referenced wind vector components with respect to the relevant variables. Then, these sensitivity terms can be combined

342 to compute the overall measurement error (1σ) in the geo-referenced 3D wind vector (Eqs. S21 to S23 in Supplement Part

343 A).

344 To estimate the errors in the geo-referenced wind vector and turbulent flux, we performed a Monte Carlo simulation of the

345 data processing procedure.

346 The Monte Carlo simulation method consists of repeated calculation of the target quantity, each time varying the input

347 data randomly within their stated limits of precision. The distribution of the calculated quantity then shows the effects of the

348 ~~imprecision of the input data (Anderson, 1976). In this study, all input variables (Table 1) used to calculate the geo-~~
349 ~~referenced wind vector and turbulent flux were randomly sampled from the Gaussian distributions with means corresponding~~
350 ~~to the constant altitude straight line flight and one standard deviation (1σ) widths given by individual component typical~~
351 ~~precision specifications from the manufacturer. Errors in the input variables are considered uncorrelated. The Monte Carlo~~
352 ~~process was repeated $N = 10^5$ times, and the measurement precision of the geo-referenced wind vector and turbulent flux~~
353 ~~was estimated as the standard deviation of the distribution of the simulated results.~~

The above wind measurement error analysis ~~Monte Carlo error simulation~~ gives the nominal measurement precision of the geo-referenced wind ~~and turbulent flux~~, but does not consider the influence of environmental changes. Following the methods of Lenschow and Sun (2007), we assess whether the accuracy of wind measurements from the UAV in satisfying the minimum signal level needed for resolving the mesoscale variations of the three wind components in the encountered atmospheric conditions. Firstly, the minimum required signal level for measurement of vertical air speed (ω) under the encountered atmospheric conditions could be estimated as (Lenschow and Sun, 2007):

$$\frac{\partial w}{\partial t} < 0.2\sqrt{2}\sigma_w 2\pi k U_a \tag{1}$$

with the true airspeed (U_a) set to mean cruise speed 30 m s^{-1}, the peak signal magnitude (σ_w) of the power spectra, and the corresponding wavenumber (k) (Thomas et al., 2012). The measurement error of the system in the vertical wind component can be calculated as (Lenschow and Sun, 2007):

$$\frac{\partial w}{\partial t} \cong \Theta \frac{\partial U_a}{\partial t} + U_a \frac{\partial \Theta}{\partial t} + \frac{\partial w_{UAV}}{\partial t} \tag{2}$$

with $\Theta = \alpha - \theta$, where α is the attack angle, θ is the pitch angle, w_{UAV} is the UAV's vertical velocity. According to Lenschow and Sun (2007), the signal level and mesoscale fluctuation of horizontal wind components (u and v) are considerably larger than that of vertical wind, so the accuracy criteria are not nearly as stringent. The measurement error of the horizontal wind component could be calculated as (Lenschow and Sun, 2007):

$$\frac{\partial u}{\partial t} \cong -\frac{\partial U_a}{\partial t} + \frac{\partial u_{UAV}}{\partial t} \tag{3}$$

$$\frac{\partial v}{\partial t} \cong \Psi \frac{\partial U_a}{\partial t} + v_{tas}\frac{\partial \Psi}{\partial t} + \frac{\partial v_{UAV}}{\partial t} \tag{4}$$

and,

$$\Psi \equiv \psi' + \beta \tag{5}$$

where u_{UAV}, v_{UAV} are the UAV's horizontal velocity measured from INS, ψ' is the departure of the measured true heading from the average true heading, and β is the sideslip angle of airflow. If the measurement error of the 3D wind vector from Eqs. (2) to (4) is smaller than the required minimum signal level of the vertical and horizontal wind components, it can be

confirmed that the measurement accuracy of the geo-referenced 3D wind vector from UAV is sufficient to resolve the mesoscale variations of the three wind components in the encountered atmospheric conditions.

~~In addition,~~ 2.4.2 Wind measurement evaluation

~~The key to successful aircraft EC measurements lies in the translation of accurately measured, aircraft-orientated, wind vectors to geo-referenced orthogonal wind vectors (Thomas et al., 2012). A~~accurate measurements of geo-referenced wind ~~vectors~~ typically not only depend on the measurement precision of the sensors (i.e., 5HP and INS), but also related to the quality of the calibration parameters~~, as well as~~ and the geometry structure of the UAV ~~based~~ EC system (i.e., flow distortion and leverage effect). For evaluation of the effect of the latter two aspects, a calibration flight campaign (Section 2.2.1) was performed to determine the calibration parameter ($\epsilon_\psi, \epsilon_\theta$), check its quality, as well as to ascertain the effects of the lever arm and up-wash by the wings. The methods for acquiring the calibration parameter were given by Vellinga et al. (2013) and Sun et al. (2021a), and the results are reported in Supplement Part C (Figs. S2 and S3). ~~In~~ During the in-flight calibration campaign, a 'racetrack' maneuver was performed to check the quality of the calibration parameters determined from the 'box' flight maneuver. The initial ($\epsilon_\psi = 0°, \epsilon_\theta = 0°$) and calibrated ($\epsilon_\theta = -0.183°, \epsilon_\psi = 2°$, in Supplement Part C) set of parameters were used to calculate the geo-referenced wind vector. By comparing the mean and standard deviation of the horizontal and vertical wind vector between the initial and calibrated set, the quality of the geo-referenced wind vector measurement in real environment conditions can be verified.

The relative wind vector ($\widehat{U}_a$) measured by the aircraft is susceptible to flow distortion because the airplane must distort the flow to generate lift and thrust, and the aircraft's propellers, fuselage, and wings are the main sources of flow distortion as flow barriers (Metzger et al., 2011). For fixed-wing aircrafts, the wind probe mounted on the nose of the UAV and extended as far forward of the fuselage as possible could avoid significant influence from flow distortion from the fuselage and propellers. Nevertheless, ~~E~~effects from the ~~flow distortion around the body of the aircraft, especially the~~ induced upwash by the wings can~~, can also significantly influence~~ significantly influence the correspondence between measured and free-stream flow variables (Garman et al., 2008). The induced upwash by the wings modifies the local angle of attack, causing the measured attack angle (α) to be larger than the free-stream attack angle (α_∞). The magnitude of upwash influence generally increases with airplane size and airspeed, typically ranging from 0.5 to 2.5 m s^{-1} as reported by the manned fixed-wing aircraft (Garman et al., 2008). Therefore, for wind measurements by manned fixed-wing aircrafts, the upwash effects must be corrected (Garman et al., 2008; Kalogiros and Wang, 2002). However, wind measurements using a multi-hole probe on the UAV seldom need this correction due to the fuselage size and because the airspeed is very low compared to a manned aircraft.

In order to access whether the lift-induced upwash could be safety ignored by the current UAV-based EC system, the 'acceleration-deceleration' flight maneuver was performed. ~~A~~According to Crawford et al. (1996), the pitch angle (θ) by the INS instrument can be utilized as an estimate of the free-stream attack angle (α_∞) if the aircraft's vertical velocity is zero,

since it is unaffected by lift-induced upwash and varies directly with α_∞ when the ambient vertical wind is zero. Under ideal conditions (zero aircraft vertical velocity and zero ambient vertical wind), the approximation relationship of $\theta \cong \alpha_\infty$ is valid when $\theta < 6°$ (Crawford et al., 1996; Vellinga et al., 2013). Departures from the 1:1 relationship can be caused by airflow distortion around the airplane behind the 5HP. The 'acceleration-deceleration' maneuver produced various pitch and attack angles measured under various airspeeds, which allowed a direct comparison between the pitch angle (θ) and the attack angle (α). If the slope between α and θ is close to unity, it indicates that the influence of lift-induced upwash can be ignored; otherwise, its influence should be corrected using upwash models (Garman et al., 2006). ~~At last~~Meanwhile, the influence of leverage effects was also evaluated based on the measurement data from the 'acceleration-deceleration' maneuver by considering or ignoring the leverage effect correction term in Eqs. (S15) to (S17).

2.4.2 Flux measurement error caused by instrumental noise

Errors or uncertainties in EC measurements can be systematic or random. Measurement from UAV, they can be attributed to several sources, mainly including instrumental noise, data handing, atmospheric conditions, insufficient flux calculation length, and bumpy flight environment (Mahrt, 1998; Finkelstein and Sims, 2001; Mauder et al., 2013). Knowledge of the measurement precision is of great importance for interpretation of EC measurements especially when detecting small fluxes in terms of turbulent exchange or signal-to-noise (SNR) of the instrumentation. Determination of the flux measurement error from instrument noise is very useful, as it is related not only to the system performance, but also to the minimum resolvable capability for the flux to be measured. In the current study, uncertainty related to instrumental noise (listed in Table 1) was estimated with a directly method proposed by Billesbach (2011). This method can be called as "random shuffle" (denoted as the RS) method and was "designed to only be sensitive to random instrument noise". According to Billesbach (2011), the uncertainty of the flux covariance can be expressed as:

$$\sigma_{\overline{w'x'}} \equiv \frac{1}{N}\sum_{i,j=1}^{N} w'(t_i)x'(t_j) \tag{6}$$

where x is the target entity of the covariance, N is the number of measurements contained in the block averaging period, $j \in [1...N]$ but the values are in the random order. The idea behind the RS method was that the randomly shuffled will remove the covariance between biophysical (source/sink) and transport mechanisms, leaving only the random "accidental" correlations attributed mostly to instrument noise (Billesbach, 2011). It means that the shuffled component x makes it uncorrelated in time/space and decorrelates x from w, resulting in two independent variables (i.e., $\overline{w'x'} \sim 0$), and any residual value of the covariance is attributed to random instrument noise. In addition to the basic assumptions made in EC flux calculation, one additional assumption in RS method is that the block averaging period should be sufficiently long to accurately represent the lowest significant frequencies contributing to the covariance which could be verified by forming Ogive plots of the covariance (Billesbach, 2011).

In this study, in order to obtain robust estimates of the instrumental noise, $\sigma_{\overline{w'x'}}$ was repeatedly calculated 20 times for every straight and level flight leg in operation flight (Fig. 2), and the mean of the absolute values of these 20 replicated

440 estimates for $\sigma_{\overline{w'x'}}$ were used to estimate the random uncertainty related to instrumental noise. According to Rannik et al.
441 (2016), RS method tends to overestimate the covariance uncertainty due to instrumental noise only. Then, the uncertainty in
442 the flux covariance of sensible heat ($\sigma_{\overline{w'T'}}$), latent heat ($\sigma_{\overline{w'\rho_v'}}$), and CO_2 ($\sigma_{\overline{w'\rho_c'}}$) were estimated using RS method,
443 respectively.
444 It should be noted that the measurement error of EC flux measurement is influenced not only by the uncertainty in the raw
445 covariance but also by the propagated errors form correction terms (i.e., WPL correction) or any lens contamination
446 (Serrano-Ortiz et al., 2008). For EC measurement from our UAV, the signal quality of the IRGA is checked before each
447 flight measurement to ensure that the measurement of gas concentration is not affected by lens contamination. The final
448 uncertainty of flux measurement was evaluated using the partial derivatives of the full flux calculation equation with respect
449 to their flux value derived by Liu et al. (2006) (Eqs. S29 to S31 in Supplement Part B). These equations (Eqs. S29 to S31)
450 ignored the perturbations terms from the errors in the individual scalar (i.e., ρ_v, ρ_c, T) which were proved negligible small
451 (Serrano-Ortiz et al., 2008). At last, after several repetitive calculation of the Eq. (6), their averaged value then be combined
452 to Eqs. (S29) to (S31) for estimating the final flux measurement error due to instrumental noise.
453

454 **2.4.3 3 Resonance effects**

455 Previous work found that the measurement of the atmospheric scalars (e.g., air temperature, H_2O, and CO_2 concentration) is
456 susceptible to resonance effects caused by the operation of the engine and propeller (Sun et al., 2021b). In order to further
457 reduce the resonance effects, the vibration damping structure of the developed UAV-based EC system was further optimized.
458 The reference (co)spectra curve of Massman and Clement (2005) was used to quantify the influence of the resonance effects
459 remaining after vibration isolation optimization. Massman and Clement (2005) gave the generalization mathematical
460 expression of the models of spectra and co-spectra:

461 $$Co(f) = A_0 \frac{1/f_x}{[1+m(f/f_x)^{2\mu}]^{\frac{1}{2\mu}(\frac{m+1}{m})}} \tag{6}$$

462 where f is frequency (Hz), f_x is the frequency at which $fCo(f)$ reaches its maximum value, A_0 is a normalization parameter,
463 m is the (inertial subrange) slope parameter, and μ is the broadness parameter. To describe co-spectra, m should be 3/4; to
464 describe spectra, m should be 3/2. According to Massman and Clement (2005), $\mu = 7/6$ under stable atmospheric condition
465 and $\mu = 1/2$ under unstable atmospheric condition. Fast Fourier transform (FFT) method was used to calculate the spectra
466 and co-spectra of the measured turbulent variables. Before calculating the turbulence (co)spectra, condition of the raw
467 turbulence data was performed, including a linear detrend and tapering using the Hamming window to reduce the spectral
468 leakage (sharp edge) according to Kaimal et al. (1989).
469 According to Sun et al. (2021b), the noise influence from resonance mainly appears in the high frequency domain,—.
470 According to the feature of spectral curve, the frequency range of the noise region was artificially designated to $f > 8$ Hz for

air temperature, $f = 1\sim5$ Hz for water vapor, and $f = 1\sim8$ Hz for CO_2. The normalized spectra and co-spectra curve were adopted and the area difference of the designated frequency range beneath the (co)spectra curve between the measured and reference (co)spectra curve was calculated to quantify the influence of resonance noise in the variance and flux_covariance of the measurement atmosphere scalars. An example is shown in Figure 3, and also shown is the reference (co)spectra curve of Massman and Clement (2005), with the (co)spectral maximum at $f_x = 0.1$. The red region in Fig. 3 represents the impact extent of the resonance noise in the variance (Figs. 3a to 3c) and flux_covariancees (Figs. 3d to 3f) of the measured scalars. The systematic noise deviation in the fluxes of sensible, latent heat and CO_2 could be derived relative to the entire frequency range.
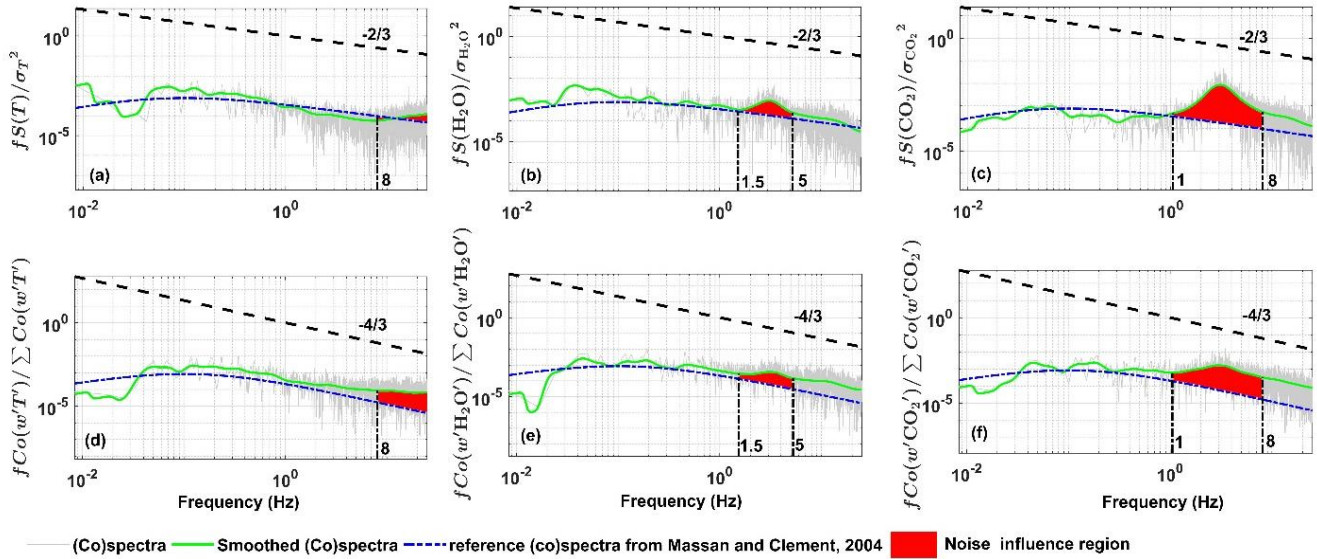
Figure 3. The influence of resonance noise on the spectra (top row) and co-spectra (bottom row) curve of the measured scalars based on the measurement from the standard operation flight campaign on 8 August 2022 at Dagang district, Tianjin, China. The red region is the area difference of the designated frequency range (vertical black dashed-dotted line) beneath the (co)spectral curve between the measured and reference (co)spectral curve.

2.4.4 Sensitivity analysis

To understand the relevance relative influence of external the calibration parameters onfor the measurements of geo-referenced wind vector and turbulent flux, two sensitivity tests were conducted. TThe magnitude of the change perturbation in the wind vector and turbulent flux was investigated as a function of the uncertainties of in the four calibration parameters, including: three mounting misalignment angles (ϵ_ψ, ϵ_θ, ϵ_ϕ) between the 5HP and the CG of the UAV and one temperature recover factor ($\epsilon_r = 0.82$) used to calculate the ambient temperature (Eq. 3 in Sun et al. 2021a).

First, the sensitivity of the geo-referenced 3D wind vector and turbulent flux to the uncertainties of the individual parameter was investigated. The geo-referenced 3D wind vector and turbulent flux was calculated based on the straight leg (about 4 km) of the standard operational flight with an by addeing and error of $\pm30\,\%$ to the optimum value of each

493 calibration parameter alternately; except for ϵ_ϕ, for which the typical range of $\pm0.9°$ was taken for sensitivity analysis

494 (Vellinga et al., 2013).

495   Then, in order to test the overall interaction between the parameters, a second sensitivity test was performed to calculate

496 the geo-referenced 3D wind vector and turbulent fluxes by adding $\pm30\%$ error to all calibration parameters

497 simultaneously.~~to test the overall interactions between the parameters, a second sensitivity test was run to calculate the geo-~~

498 ~~referenced 3D wind vector and turbulent flux using an error of ±30 % added to all the calibration parameters simultaneously.~~

499 Lastly, their relative errors (*RE*) with respect to the original value were ~~the relative errors of the calibrated set and the added~~

500 ~~error set of geo-referenced 3D wind vector and turbulent flux values was~~ calculated to evaluate the perturbation of the wind

501 vector and turbulent flux under the variation of each calibration parameter as well as under simultaneous variation of all

502 calibration parameters. During the sensitivity analysis, the calculated geo-referenced wind and turbulent flux results whose

503 absolute value was less than their least resolvable magnitude ~~(in Table 2)~~ were filtered out to avoid the influence of the

504 errors contained in the measurements themselves on the results.

505 ~~ing the error contained in the measurement itself from impacting results.~~

2.4.5 Relative error

507 In this study, relative error (*RE*) was used to evaluate the influence of different factors on the measurements of geo-

508 referenced wind vector and turbulent flux by the UAV-based EC system. It is defined as:

509 $RE = \frac{|x_0| - |x|}{|x|} \times 100\%$ (7)

510 where '| |' means the absolute value, x is the 'true' value, x_0 is the influenced value. *RE* > 0 means the exerted influence will

511 cause the measurement value to be larger than 'true' value and vice versa.

3 Results

513 **3.1 Wind measurement evaluation~~Error analysis~~**

514 Evaluation of the wind measurement performance from the UAV-based EC system includes three contents: (1) measurement

515 precision and its ability to resolve the mesoscale variations of the wind, (2) checking the quality of the acquired calibration

516 parameters, and (3) checking whether the measured wind vector is affected by upwash flow and leverage effects.

517   First, according to the equations described in Supplement Part A (Eqs. S18 to S23), the measurement precision for

518 horizontal wind components is a function of true airspeed and true heading, while, the measurement precision for vertical

519 wind component is largely decided by the true airspeed. The typical values of true airspeed ranging from 25 m s^{-1} to 35 m s^{-1}

520 (interval of 1 m s^{-1}) and the true heading values ranging from 0° to 180° (interval of 30°) were used in the evaluation of

521 wind measurement error. Then, the measurement precision (1σ) of the geo-reference 3D wind vector from aircraft was

estimated using the measurement precision of the related parameters from Table 1. The results are shown in Figure 4 for the measurement precision of horizontal wind (σ_u and σ_v in Figs. 4a and 4b) and vertical wind (σ_w in Fig 4c), respectively. The typical values of the measurement precision are ranging from 0.05 m s^{-1} to 0.07 m s^{-1} for horizontal wind component u, ranging from 0.02 m s^{-1} to 0.08 m s^{-1} for horizontal wind component v, and ranging from 0.05 m s^{-1} to 0.07 m s^{-1} for vertical wind component w. When the flight direction is towards due east or due west, the horizontal wind (u and v) has the smallest measurement error.
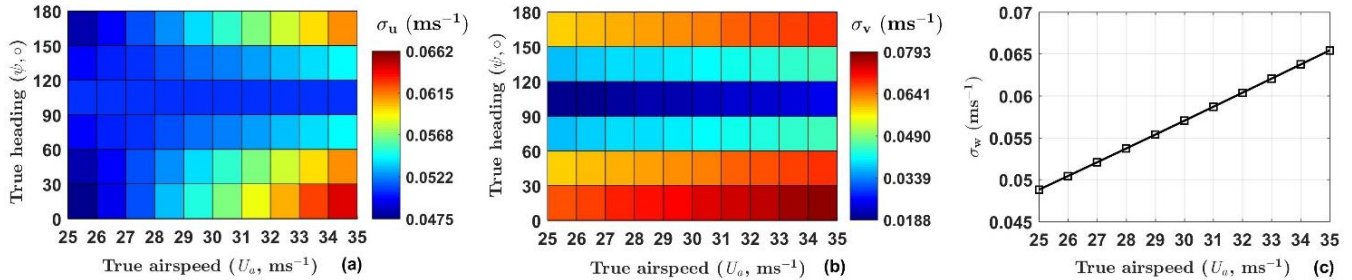
Figure 4. Estimated measurement precision (1σ) of the horizontal wind (a, b) and vertical wind (c) according to the equations described in Supplement Part A (Eqs. S18 to S23).

Generally speaking, an autopiloted UAV can maintain a near-constant true airspeed during the cruise flight phase. For a true airspeed of 30 m s^{-1} for the current UAV-based EC system during the cruising, the maximum measurement error in the northward, eastward, and vertical velocities of the geo-referenced wind components were calculated as approximately 0.06, 0.07, and 0.06 m s^{-1}, respectively. Then, we assume that a minimum signal-to-noise ratio of 10:1 is required to measure the wind components with sufficient precision for EC measurements (Metzger et al., 2012). Accordingly, in the real environments, horizontal and vertical wind speed greater than 0.7 m s^{-1} and 0.6 m s^{-1} can be reliably measured, respectively (Table 2).

After running $N = 10^5$ samples through the data processing procedure, the results of Monte Carlo error simulation for geo-referenced wind vector and turbulent flux are summarized in Table 2. The least resolvable magnitude of the measurements of wind and turbulent flux was calculated by assuming the minimum required signal-to-noise ratio of 5:1 (Metzger et al., 2012). The 1σ precision of the geo-referenced wind vector measurement was ± 0.04 m s^{-1} for the horizontal and vertical wind components, and the magnitude of the wind velocity greater than 0.2 m s^{-1} could be reliably measured. The calculated measurement 1σ precision of the geo-referenced vertical wind component agreed well with the 1σ uncertainty in the vertical wind measurement (0.057 m s^{-1}) calculated by propagating instrument errors through linear combination, as described by Sun et al. (2021a).

Table 2: The maximum measurement error in the northward (u), eastward (v), and vertical (w) velocities of the geo-referenced wind components at the true airspeed of 30 m s^{-1}, Results of the simulated measurement precision (1σ) of the geo-

548 ~~referenced wind vector and turbulent flux from the Monte Carlo error simulation with N=10⁵ runs~~ and the least resolvable

549 magnitude assuming the minimum required signal-to-noise ratio of 10~~5~~:1.

Measurements	Measurement precision (1σ)	Least resolvable magnitude
u-windspeed (m s^{-1})	0.06~~4~~	0.6~~2~~
v-windspeed (m s^{-1})	0.07~~3~~	0.7
w-windspeed (m s^{-1})	0.06~~4~~	0.6~~2~~
~~CO_2 flux (μmol m^{-2} s^{-1})~~	~~0.08~~	~~0.4~~
~~Sensible heat flux (W m^{-2})~~	~~1.61~~	~~8.05~~
~~Latent heat flux (W m^{-2})~~	~~0.15~~	~~0.75~~
~~Friction velocity (m s^{-1})~~	~~0.02~~	~~0.1~~

550 ~~The simulated 1σ measurement precision of the turbulent flux was 0.08 μmol m^{-2} s for the CO_2 flux, 1.61 W m^{-2} for the~~

551 ~~sensible heat flux, 0.15 W m^{-2} for the latent heat flux, and 0.02 m s^{-1} for the friction velocity, respectively. Using a signal-to-~~

552 ~~noise ratio of 5:1, the minimum magnitudes for reliably resolving the CO_2 flux, friction velocity, sensible and latent heat~~

553 ~~fluxes were 0.4 μmol m^{-2} s, 0.1 m s^{-1}, 8.05 W m^{-2}, and 0.75 W m^{-2}, respectively.~~

554 The ~~Monte Carlo error simulation~~above results gave the nominal precision for wind measurements that does not consider

555 the influence of environmental conditions. Changes in the environment will lead to sensor drift, increasingly deteriorating

556 the measurement with flight duration (Metzger et al., 2012; Lenschow and Sun, 2007). Following the methods of Lenschow

557 and Sun (2007), the ability of the limitations of the accuracy of wind field measurements from UAV to resolve the mesoscale

558 variations of the 3D wind components in the encountered atmospheric conditions was assessed. For the vertical wind, the

559 mesoscale variability was defined as the peak signal magnitude of the power spectra curve. The corresponding average

560 wavenumber was determined as 0.09 m^{-1} based on the straight flight leg (about 4 km, lasting about 120 s) of the standard

561 operational flight. Then, the minimum required signal level for the vertical wind measurement was estimated as $\partial w / \partial t \simeq$

562 0.14 m s^{-2}. The accuracy of the vertical wind measurement using Eq. (2) is estimated as follows. The first term on the right-

563 hand side of Eq. (2) is dominated by the drift in the differential pressure transducer, the value of $\partial U_a = 0.05$ m s^{-1} acquired

564 from the wind tunnel test was applied (Table 1). The histogram of Θ derived from the standard operational flights is shown

565 in Figure 4~~5~~. The 99 % confidence interval indicates that the value of Θ seldom exceeds $\pm 3°$, i.e., ± 0.053 radians. Thus, the

566 value of the first term was estimated as 2.2×10^{-5} m s^{-2}.

567
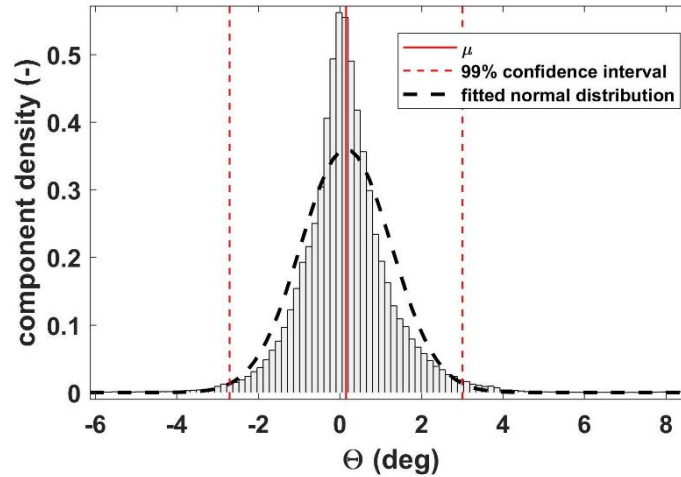
Figure 54. Histogram of Θ derived from the standard operational flight. Component density is scaled so that the histogram has a total area of one. Red vertical lines indicate distribution average (solid) and 99% confidence interval (dashed). The black dashed bell curve displays a reference fitted normal distribution.

The second term in Eq. (2) is a combination of INS pitch accuracy and drift in the measured attack angles. The combined accuracies of these two sensors were applied to derive $\partial\Theta = 0.0024$ radians. Thus, the second term in Eq. (2) was estimated as 6×10^{-4} m s^{-2}. Finally, the third term in Eq. (2) was estimated as 1.7×10^{-4} m s^{-2}, according to the stated accuracy of the vertical velocity from the INS. The overall performance of the vertical wind measurement (7.9×10^{-4} m s^{-2}) was accurate enough to resolve the mesoscale variations in vertical air velocity.

The required accuracy of horizontal wind for mesoscale measurement was estimated as 10 times larger than that of vertical wind, i.e., $\partial u/\partial t \simeq \partial v/\partial t \simeq 1.4$ m s^{-2}. The measurement accuracy of the horizontal wind component u was estimated as 4.8×10^{-4} m s^{-2} according to Eq. (3). Like the first term in Eq. (2), with the value of Ψ rarely exceeding ± 0.18 radians, the measurement accuracy of the horizontal wind component v was estimated as 2.7×10^{-2} m s^{-2} according to Eq. (4). Thus, the measurement accuracy of the horizontal wind components was accurate enough to resolve the mesoscale variations in the horizontal air velocity as well.

~~3.2 Wind measurement~~

Second, before checking the quality of the acquired calibration parameters, ~~T~~the calibration results of the offset in pitch (ϵ_θ) and heading (ϵ_ψ) angles based on the 'box' maneuver are provided in Supplement Part C (Figs. S2 and S3). The final calibration values are $\epsilon_\theta = -0.183°$ and $\epsilon_\psi = 2°$. In order to verify the quality of these calibration parameters, a 'racetrack' maneuver was performed. Figure ~~5~~6 shows the verification results by plotting wind vector~~s~~ and calculating summary statistics for the 'racetrack' maneuver (including turns), using the initial ($\epsilon_\theta = \epsilon_\psi = 0°$, Fig. ~~5a~~6a) and calibrated (Fig. ~~5b~~6b) set of parameters. The introduction of the calibration parameter effectively improved the quality of geo-referenced wind vector measurement. The standard deviation for wind direction, $\sigma_{U_{dir}}$, is 4.9° for the calibrated set compared to 8.7° for the

590   initial set, and the standard deviation of wind speed, σ_U, is 0.52 m s^{-1} for the calibrated set compared to 1.12 m s^{-1} for the

591   initial set. The average vertical wind speed is much closer to zero ($\overline{w} = -0.006$ m s^{-1}) for the calibrated set than for the

592   initial set ($\overline{w} = 0.1$ m s^{-1}). For the horizontal wind, it is evident from Fig. 5 6 that the wind direction and velocity are little

593   affected by sharp turns. On the contrary, the measurement of the vertical wind component is obviously affected by turns in

594   flight, as shown by the large ripple in the vertical wind speed around the scan value of 150 (Fig. 56). It should be noted that

595   the influence of upwash flow and the leverage effect are not considered in the calculated of geo-referenced wind vector.
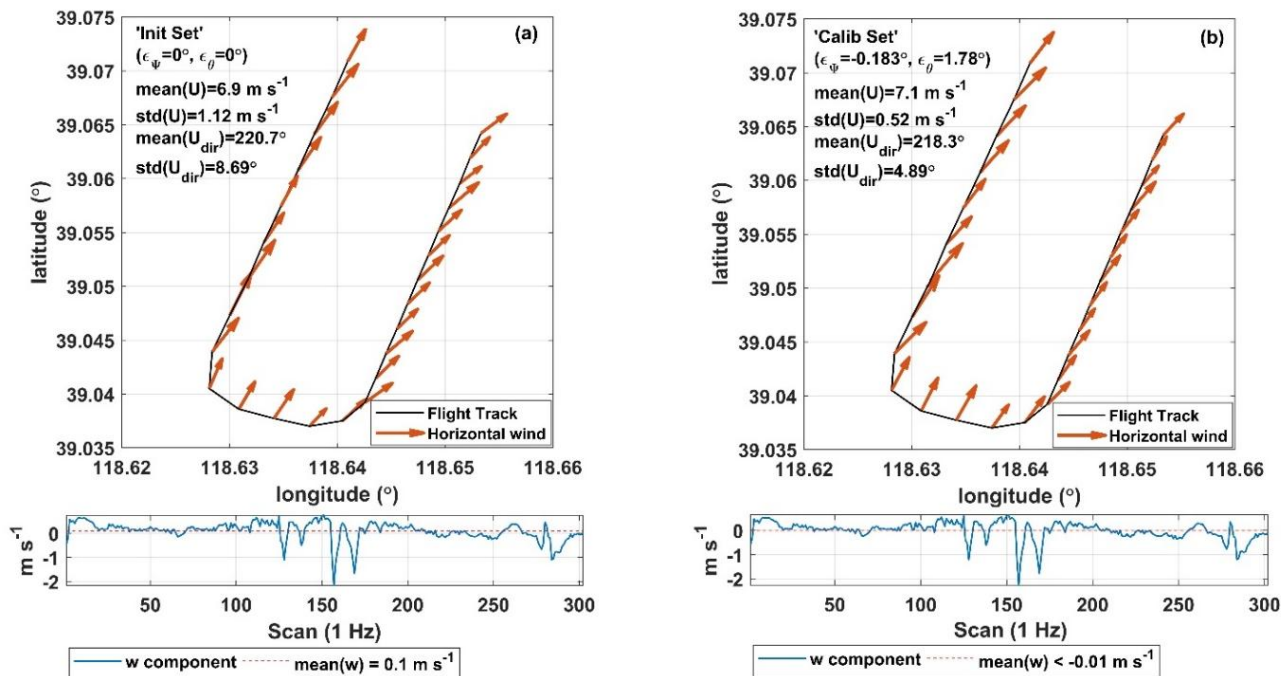
596

597   **Figure 56. Quality check of the calibration parameter by plotting wind vectors and calculating summary statistics for the**
598   **'racetrack' maneuver, using the initial (a) and calibrated (b) set of parameters. The calibration flight was carried out on 4**
599   **September 2022 at the Caofeidian Shoal Harbor.**

600   Third, Iin order to check the influence of the lift-induced upwash on the attack angle measurement from the 5HP, an

601   'acceleration-deceleration' flight maneuver was performed. During the 'acceleration-deceleration' maneuver, INS data

602   shown a vertical velocity of the UAV at 0.05±0.2 m s^{-1}, the altitude of UAV at 392±0.6 m, the heading of UAV at 199±2.4° .

603   The flight conditions met the requirements of the 'acceleration-deceleration' maneuver (Vellinga et al., 2013). The

604   relationship between the pitch angle (θ) measured by INS and the attack angle (α) measured by 5HP is plotted in Figure 6 7,

605   where the attack angle was not corrected for lift-induced upwash. The slope (0.94) between θ and α is close to its theoretical

606   value of 1, and the intercept (0.16) is close to zero. This result indicates that the lift-induced upwash has only a very small

607   effect on the attack angle, and the influence of upwash could be ignored.
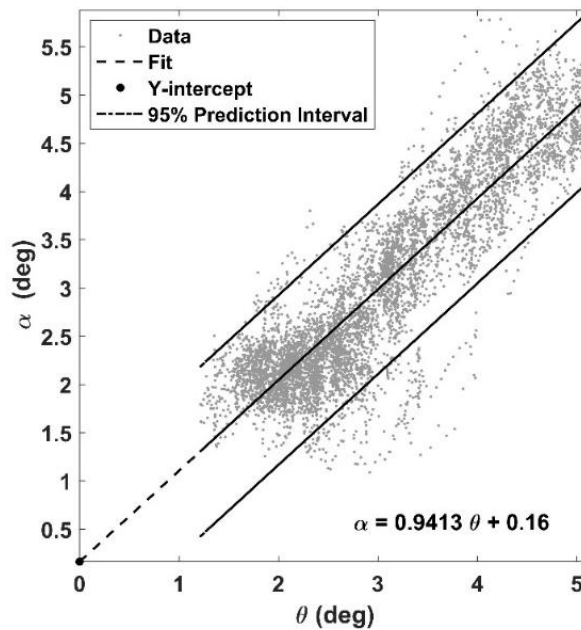
608

609 **Figure 67. Relationship between the pitch angle (θ) measured by INS and the attack angle (α) measured by 5HP. The fitted linear**
610 **equation is also shown.**

611   Finally, the geo-referenced wind vector was calculated with and without the correction for the leverage effect based on the
612 measurement data from the 'acceleration-deceleration' flight maneuver. The average relative differences between the
613 corrected and uncorrected horizontal and vertical wind speeds are 0.1 % and 0.2 %, respectively. The standard deviation for
614 horizontal wind speed is 0.307 m s^{-1} without the level arm term compared to 0.306 m s^{-1} when the level arm term is
615 introduced. The standard deviation of vertical wind speed is 0.254 m s^{-1} without the level arm term compared to 0.253 m s^{-1}
616 with the level arm term. The correction of leverage effect had minimal effect on improving the geo-referenced wind vector
617 measurement; therefore, this correction term can be ignored.

618 **3.2 Flux measurement error caused by instrumental noise**

619 Flux measurement error caused by the instrumental noise gives the lowest limit of the flux that the UAV-based EC system is
620 able to measure. Such measurement error was assessed by combining the covariance uncertainty estimated by RS method
621 and the propagation of errors in flux correction terms. Before estimating the flux covariance uncertainty using RS method,
622 using the measured data from each straight and level flight leg of the standard operational flight (Fig. 2), the normalized
623 integrated cospectra (ogives) curves of sensible heat (Fig. 8a), latent heat (Fig. 8b), and CO_2 (Fig. 8c) flux are formed as a
624 function of wavenumber (k), where $k = 2\pi f / U_a$. As shown in Figure 8, although the heterogeneous turbulence (or
625 mesoscale turbulence) interfered the shape of ogive curves, most curves converged at the high and low frequency ends,
626 which indicated that these segmented data were sufficiently long to represent the lowest significant frequencies contributing
627 to the covariance.
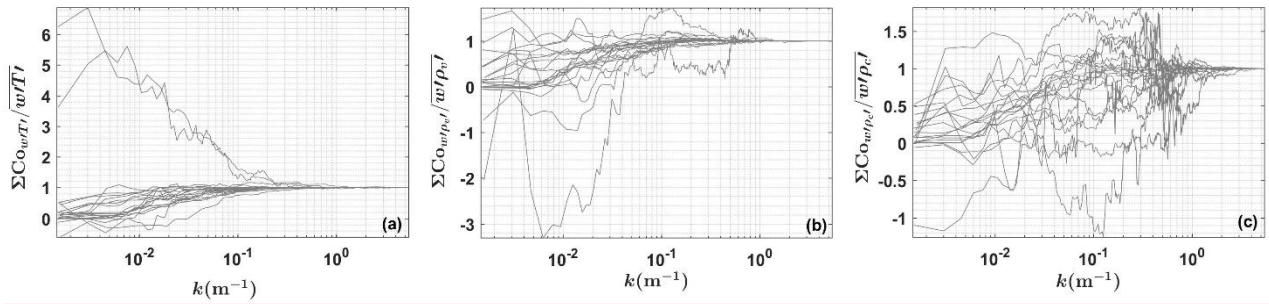
628

629 **Figure 8. Normalized ogive curves as a function of wavenumber for the flux covariance of sensible heat (a), latent heat (b), and**
630 **CO_2 (c) from each straight and level flight leg of the standard operational flight in Section 2.2.2.**

631   Then, the results of instrumental noise related relative flux measurement error compared to the magnitude of the flux are
632 shown in Figure 9. It can be seen that the flux measurement error caused by instrumental noise significantly decreases when
633 the flux magnitude increases. It is not surprising since, in theory, instrumental noise is usually close to a constant and the
634 relative flux measurement error caused by instrumental noise will decreases with increasing measurement magnitude.
635 Overall, instrumental noise has the least effect on latent heat flux (ranging from 0.02% to 2.42% in this study) measurements,
636 followed by sensible heat flux (ranging from 0.05% to 8.6% in this study), and has the greatest effect on the measurement of
637 CO_2 flux (ranging from 0.22% to 75.6% in this study). Then, a simple rational function relationship between the relative
638 measurement error and the flux magnitude is fitted according to the measured data, where the constant term in the
639 denominator is set to 0. The fitted coefficient in the numerator can be considered as the flux measurement error caused by
640 instrumental noises, which are 0.03 $\mu mol\ m^{-2}\ s^{-1}$, 0.02 $W\ m^{-2}$, and 0.08 $W\ m^{-2}$ for the measurement of CO_2 flux, sensible and
641 latent heat flux, respectively. At last, using the signal-to-noise ratio of 10:1, the minimum magnitudes for reliably resolving
642 the CO_2 flux, sensible and latent heat fluxes were estimated as 0.3 $\mu mol\ m^{-2}\ s^{-1}$, 0.2 $W\ m^{-2}$, and 0.8 $W\ m^{-2}$, respectively.
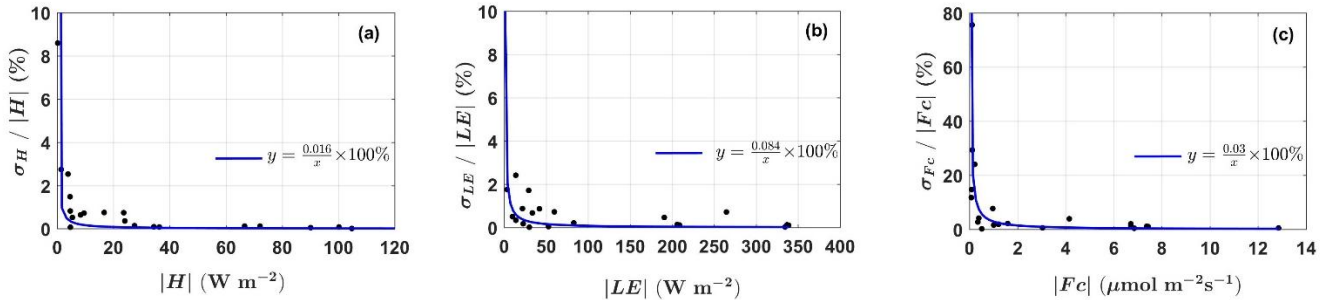
643

644 **Figure 9. Relative flux measurement error caused by instrumental noise plotted against the magnitude of the flux. Also shown the**
645 **fitted error curves. Measured data was from the standard operation flights in Section 2.2.2.**

646

3.3 Resonance noise

The resonance noise from the engine and propeller can lead to systematic overestimation of the variance and covariance of the observed atmospheric scalars. Since the noise mainly appears in the high frequency domain of the (co)spectra, the reference (co)spectral curve of Massman and Clement (2005) was used to quantify the systematically bias caused by the resonance noise.

All spectra curves of the variance of measured scalars (including air temperature, H_2O, and CO_2 concentration) approximately followed the reference spectra curve and the reference -2/3 slope in the inertial subrange (Figs. 3a to 3c). The largest scatter occurred in the spectra of CO_2 (Fig. 3c). When comparing the spectra curve with the reference spectra, the resonance noise led to a systematic deviation in the variance of air temperature, H_2O, and CO_2 concentration of 0.1±0.1 %, 1.0±0.79 %, and 4.4±0.66 %, respectively, relative to the entire frequency range. For the flux ~~covariances~~ covariance of sensible, latent heat and CO_2, all the co-spectra curves approximately follow the reference co-spectra curve and the reference -4/3 slope in the inertial subrange (Figs. 3d to 3f). Compared with the reference co-spectra, the resonance noise led to a systematic deviation in the flux of sensible, latent heat, and CO_2 of 0.07±0.004 %, 0.3±0.25 %, and 2.9±1.62 %, respectively, relative to the entire frequency range.

The results show that the resonance noise has a very little impact on the measured variance and flux ~~covariances~~ covariance. Among them, the measurements of CO_2 concentration and flux are most susceptible to the resonance noise, but the impact of this noise is limited to around 5 % of the observed value.

3.4 Sensitivity analysis

In this study, in order to investigate the relevance of the calibration parameters for the measurement of the ~~sensitivity of the~~ geo-referenced wind vector and turbulent flux ~~measurements to the uncertainties of the external calibration parameter~~, two ~~a~~ sensitivity tests ~~were~~ as conducted by adding an error of ±30 % to the used optimum parameters (ϵ_ψ, ϵ_θ, ϵ_ϕ, ϵ_r). ~~calibrated value of each calibration parameter.~~ ~~We~~ It is assumed that the maximum uncertainties contained in the calibration parameter is not more than 30 % of its own value.

First, the sensitivity of the geo-referenced 3D wind and turbulent flux to the uncertaint~~yies~~ ~~in~~of the individual parameter~~s~~ was tested. The RE value is~~was~~ used to quantify the sensitivity~~.~~, ~~Tables 3 and 4 show the~~and the RE results are summarized in Tables 3 and 4. For the measurement of the geo-referenced wind vector, Table 3 shows that the uncertaint~~yies~~ in the temperature recovery factor (ε_r) and 5HP mounting misalignment error in the roll (ϵ_ϕ) angle do not contribute significantly to errors in the wind measurements, which were typically smaller than 4% of the observed value in this study. ~~P~~The ~~p~~parameter ε_θ had the largest effect on the vertical wind component (up to 30 %), whereas ε_ψ had the largest effect on the horizontal wind component. For the measurement of turbulent flux~~es~~, Table 4 shows that the errors in ε_r and ϵ_ϕ does not significantly influence ~~significantly~~ the flux measurements ~~(,~~ typically small than 5% of the observed value in this study~~)~~. The uncertainties in ~~C~~calibration parameter~~s~~ ε_θ and ε_ψ had significant effects on the measurement of turbulent flux. Adding

679 an error of ±30 % to ~~the calibration parameter~~ ε_θ ~~may~~ result in significant perturbation (large *RE* variance)~~uncertainty~~ in the
680 measured turbulent fluxes including sensible heat, latent heat and CO_2 ~~(large *RE* variance)~~. While, errors in ε_ψ to some
681 extent mainly affect the measurement of ~~Similarly, adding an error of ±30 % to the calibration parameter ε_ψ resulted in the~~
682 ~~largest effect on~~ latent heat fluxes (*RE* may up to 15 %).

683 **Table 3**: *RE* of the sensitivity test for the geo-referenced 3D wind vector (u, v, w). An error factor of ±30 % was added to
684 each calibrated parameter. The geo-referenced 3D wind vector was calculated based on the straight leg of the standard
685 operational flight.

Parameter	Error (%)	*RE* of geo-referenced 3D wind vector mean ± std		
		u (%)	v (%)	w (%)
ε_r	-30	0.04±0.41	-0.004±2	0±0
	30	0.06±0.43	0.27±1.1	-0.07±0.23
ε_φ*	-30	0.41±2.51	-0.09±2.05	1.15±2.43
	30	-0.43±2.61	0.09±1.79	-1.1±2.66
ε_θ	-30	0.03±0.41	-0.35±2.54	-30.51±6.42
	30	0.05±0.45	0.42±1.82	30.37±6.61
ε_ψ	-30	2.98±25.06	-2.04±16.3	0±0
	30	-2.97±24.96	2.42±16.63	0±0

686 * The optimum calibration value is set to 0, ε_φ was varied over ±0.9°, which is 30 % of its typical range.

687 **Table 4**: *RE* of the sensitivity test for the turbulent fluxes. An error factor of ±30 % was added to each calibrated parameter.
688 The turbulent fluxes were calculated based on the straight leg of the standard operational flight.

Parameter	Error (%)	*RE* of turbulent flux mean ± std			
		~~fCO2~~ Fc (%)	H (%)	LE (%)	u* (%)
ε_r	-30	1.04±3.04	-0.76±4.82	0.1±0.29	0±0
	30	-1.0±3.3	0.74±4.8	-0.1±0.29	0.2±1.07
ε_φ*	-30	0.07±1.2	0.03±0.7	0.15±1.51	0.54±1.71
	30	-0.14±0.89	-0.06±0.7	-0.16±1.46	0.12±1.61
ε_θ	-30	-3.27±11.18	-0.8±9.48	0.19±11.91	-4.08±5.61
	30	2.34±10.52	-0.44±8.24	-1.27±9.92	3.73±4.53
ε_ψ	-30	1.78±5.18	-0.73±4.87	1.89±13.42	0.63±5.75
	30	-0.99±3.96	-0.57±3.26	2.66±11.76	-0.59±4.42

689 * See Table 3.

690 The second sensitivity test was performed to evaluate the overall interaction between calibration parameters and the
691 calculation of geo-referenced wind vector and turbulent flux by adding an error of ±30 % to all the calibration members
692 simultaneously. ~~overall sensitivity of the geo-referenced 3D wind vector and turbulent flux to the external calibration~~
693 ~~parameters was tested by adding an error of ±30 % to all the calibration members simultaneously.~~ Tables 5 and 6 provided a
694 summary of the *RE* results from the second sensitivity test. For the measurement of geo-referenced wind vector (Table 5),

adding an error of ±30 % to ~~all~~ the calibration ~~parameters~~set at the same time resulted in ~~great perturbations to both the horizontal (low *RE* with high variance) and vertical wind components (high *RE* with low variance). For the measurement of turbulent fluxes, 30% error in the calibration parameters can result in errors in measured fluxes more than 10%. In addition, Table 6 reveals that the~~ a high *RE* (near 30 %) for vertical wind and a low *RE* (about 4%) for horizontal wind, which also had high *RE* variance (up to 28 %). For the measurement of turbulent fluxes, the measurement of the ~~latent heat flux (mean *RE* > 6 %)~~ is more sensitivity to the errors in the calibration parameter than other ~~flux~~ measurements ~~(higher mean and variance of the *RE* compared to other measurements)~~(mean *RE* < 3 %) and had a larger *RE* variance (>10 %). In general, CO2 and sensible heat fluxes as well as friction velocity are not sensitive to errors in the external calibration parameters, but there were also some exceptions where the response to errors was large (e.g., the *RE* variance of CO2 flux up to 10 %).

Table 5: *RE* of the sensitivity test for the geo-referenced 3D wind vector (u, v, w) calculated by adding an error of ±30 % to all the calibrated parameter simultaneously. The geo-referenced 3D wind vector was calculated based on the straight leg of the standard operational flight.

Parameter	Error (%)	*RE* of geo-referenced 3D wind vector mean $\pm$ std		
		u (%)	v (%)	w (%)
All	-30	4.24$\pm$27.89	-3.2$\pm$21.1	-29.35$\pm$4.63
	30	-4.15$\pm$27.46	3.55$\pm$21.91	29.16$\pm$4.86

Table 6: *RE* of the sensitivity test for the turbulent flux calculated by adding an error of ±30 % to all the calibrated parameter simultaneously. The turbulent flux was calculated based on the straight flight leg of the standard operational flight.

Parameter	Error (%)	*RE* of turbulent flux mean $\pm$ std			
		~~fCO_2~~ F_c (%)	H (%)	LE (%)	u^* (%)
All	-30	-1.19$\pm$10.51	-0.9$\pm$8.06	2.71$\pm$13.91	-2.92$\pm$8.19
	30	-0.49$\pm$10.01	-1.66$\pm$5.4	-6.07$\pm$13.24	1.74$\pm$6.55

4 Discussions

As one in a new generation of airborne flux measurement platforms, the UAV-based EC system can significantly reduce the cost of implementing airborne flux measurement campaigns and greatly promote their wide application at regional scales. ~~The trend of sensor miniaturization further promotes the rapid development of technology in this field. Sun et al. (2021a) developed an UAV-based EC system for measuring the turbulent flux of sensible heat, latent heat, CO2, as well as radiation fluxes of net radiation and photosynthetically active radiation (PAR).~~ The current~~is~~ study aimed to ~~quantitatively~~ evaluate the basic performance of th~~is system~~e UAV-based EC system developed by Sun et al. (2021a) in the measurement of wind vector and turbulent flux.

First, the wind measurement precision (nominal precision) of the UAV-based EC system was ~~evaluated~~ estimated by propagating the sensor errors to the geo-referenced wind vector ~~and turbulent flux~~ using the linearized Taylor series

719 expansions from Enriquez and Friehe (1995) ~~Monte Carlo error simulation~~. The 1σ precision ~~for~~ of geo-referenced wind

720 measurement was estimated to be $\pm 0.$~~04~~ 07 m s^{-1}, and the least resolvable magnitude for wind measurement was estimated

721 at 0.7 m s^{-1} by assuming the minimum signal-to-noise ratio of 10:1. ~~1σ precision for turbulent flux was 0.08 μmol m^{-2} s for~~

722 ~~the CO$_2$ flux, 1.61 W m^{-2} for the sensible heat flux, 0.15 W m^{-2} for the latent heat flux, and 0.02 m s^{-1} for the friction velocity.~~

723 ~~As proposed by Lenschow and Sun (2007), a minimum signal-to-noise ratio of 5:1 was assumed to be required to measure~~

724 ~~the wind field and turbulent flux. Using that ration, the least resolvable magnitude for wind and turbulent flux measurement~~

725 ~~was estimated at 0.2 m s^{-1} for wind velocity, 0.4 μmol m^{-2} s for the CO$_2$ flux, 8.05 W m^{-2} for the sensible heat flux, 0.75 W~~

726 ~~m^{-2} for the latent heat flux, and 0.1 m s^{-1} for the friction velocity.~~ The~~se~~ derived wind measurement minimum resolvable

727 magnitude~~s for measurements~~ ~~of wind vector and turbulent flux~~ can be used as a basic reference for ~~the~~wind measurement

728 capability of the UAV-based EC system, and the measured values of wind vector ~~and scalar fluxes~~ smaller than the

729 minimum resolvable values should be considered unreliable. The accuracy of the sensors was also assessed by examining the

730 collected data in the real environment (Lenschow and Sun, 2007; Thomas et al., 2012). Our results revealed that ~~T~~the overall

731 performance of geo-referenced wind measurement is sufficient accuracy for resolving the mesoscale variations of the 3D

732 wind components under the encountered atmospheric conditions. Therefore, it is possible to capture the mesoscale variability

733 of the atmospheric boundary layer (ABL) over a wide range of spatial scales by performing longer flight paths.

734 Second~~Second~~, based on the measurement data from the in-flight calibration campaign, several key factors affecting the

735 accuracy of geo-referenced wind measurement were analysed. First, the UAV-based EC system was calibrated (in

736 Supplement Part C) using measured data from the 'box' flight maneuver to correct the mounting misalignment between the

737 5HP and the CG of the UAV in the heading ($\epsilon_\theta = -0.183°$) and pitch ($\epsilon_\psi = 2°$) angles. The quality of the acquired

738 calibration parameter~~s~~ was verified using the 'racetrack' flight maneuver, and the acquired calibration value effectively

739 improved the observed wind field with smaller variance compared with the wind calculated using their initial value. ~~The~~

740 ~~measured geo-referenced 3D wind vector was consistent with the assumptions made about the atmospheric condition for~~

741 ~~calibration campaign (constant horizontal wind and near zero mean vertical wind) especially in the standard operation flight.~~

742 At the same time, ~~T~~the measurement of the vertical wind component was significantly affected by the in-flight turn

743 (maintaining about 20° roll). Therefore, it is necessary to avoid using the measured data from the turn section for turbulent

744 flux calculation. Compared to ~~the~~ other studies (Vellinga et al., 2013; Reineman et al., 2013), the relatively large variance in

745 the ~~calibrated~~ horizontal wind and wind direction after calibrated in this study may be caused by the nonstationary condition

746 of the turbulence. This was caused by the reason that the flight altitude of 400 m was not high enough to totally avoid

747 interaction from the underlying surface.

748 The current calibration procedure did not include methods to determine the offset angle in roll (ε_φ) and the temperature

749 recovery factor (ε_r) because of the small vertical separation (27.3 cm) between the 5HP and the roll axis of the UAV and the

750 small Mach number (<0.1) during operational flight. The default ($\varepsilon_\varphi = 0°$) and empirical ($\varepsilon_r = 0.82$) value were adopted for

these two~~ese~~ calibration parameters. The sensitivity analysis shown these two parameters have no large effect on the wind vector and turbulent flux.

It should be noted that ~~W~~wind measurements from the airborne platform may be susceptible to flow distortion and rigid-body rotation (leverage effects). ~~However~~Generally, the influence of these two ~~aspects~~ factors were ignored by UAV platform when calculating the geo-referenced wind vector. To confirm that these effects could be safely ignored, data from 'acceleration-deceleration' flight maneuver was used to analyse the effects of lift-induced upwash and the leverage effect on the wind measurements. ~~Our~~The results demonstrate that the upwash has almost no effect on the wind measurement, which was indicated by the near 1:1 relationship (0.94 in Fig. 7) between the measured attack angles and pitch angle. The slight departures from the ideal 1:1 relationship may have been caused by the nonstationary condition during the flight. For the influence from the leverage effects, the ~~D~~differences in 3D wind vector between corrected and uncorrected for the leverage effect is very small. ~~were very minor between the 3D wind vector corrected and uncorrected for the leverage effect.~~ Thus, ignoring the influence of the leverage effect has almost no effect on the measurement of wind. Therefore, we concluded that the geo-referenced 3D wind vector can be measured reliably by the current UAV-based EC system without considering the ~~possible disturbance~~interference from the lift-induced upwash and leverage effect ~~as indicated by the result~~s.

Third, instrumental noise related relative flux measurement error was estimated by combining the covariance uncertainty estimated by RS method and the propagation of errors in flux correction terms. By assuming that the instrumental noise is close to a constant, we fitted a simple rational function relationship between the relative measurement error and the flux magnitude according to measured data (Fig. 9), and the fitted coefficient in the numerator can be considered as the flux measurement error caused by instrumental noises. The estimated flux measurement error of CO_2, sensible and latent heat flux are 0.03 μmol m^{-2} s^{-1}, 0.02 W m^{-2}, and 0.08 W m^{-2}, respectively. Since the RS method directly uses the shuffled raw measurement data to calculate the instrumental noise induced flux measurement error, its estimated results inevitably included the effects of resonance noise from the UAV. Using the signal-to-noise ratio of 10:1, the least resolvable magnitude for turbulent flux measurement was estimated to be 0.3 μmol m^{-2} s^{-1} for the CO_2 flux, 0.2 W m^{-2} for the sensible heat flux, 0.8 W m^{-2} for the latent heat flux, respectively.

~~Third~~Fourth, because the UAV-based EC system has not completely insulated the noise from the operation of the engine and propeller and its effect on the measured scalars, the reference (co)spectra of Massman and Clement (2005) was used to quantify the effect of the resonance noise on the variance and flux of the measured scalars. Previous studies found that the influence of resonance noise mainly appears in the high frequency domain of the power spectra of the measured atmospheric scalars (e.g., air temperature, H_2O, and CO_2 concentration). The frequency range of the noise region was artificially designated for air temperature, water vapor and CO_2. By calculating the area difference of the designated frequency range beneath the (co)spectral curve between the measured and reference (co)spectral curves, the resonance effect could be quantified. The results shown that, overall, resonance noise has little impact on the variance and flux covariance~~es~~ of the measured scalars. The measurements of CO_2 concentration and its flux covariance were the most susceptible to resonance

785 noise, but the maximum effect was less than 5 %. It should be noted that this method may overestimate the deviation caused

786 by resonance noise as indicated by the reference (co)spectra curve and the measured (co)spectra not fully overlapping in the

787 inertial subrange (shown in Fig. 3).

788 In general, ~~G~~gas detection based on optical absorption methods can achieve fast and high precision gas concentration

789 measurements, but they are extremely sensitive to vibration noise. However, due to the limited space inside the UAV, it is

790 difficult to install all the hardware needed for a complex vibration isolation structure to effectively isolate the impact of

791 vibration on the gas analyser. The weight and the aerodynamic shape of the UAV also present challenges. In the future, a

792 new UAV-based EC system based on a pure electric UAV ~~could~~ will be developed. The electro-powered UAV has similar

793 performance to the current fuel-powered UAV but can minimize the impact of vibration noise from the engine and propeller

794 rotation, which makes it possible to completely isolate the resonance effect using a simple vibration isolation structure.

795 Electro-powered UAVs also have other advantages including larger wingspan (lower cruising speed), a constant CG position,

796 and lower operational complexity compared to the current system.

797 ~~Forth~~Fifth, two~~a~~ sensitivity tests ~~w~~were~~as~~ conducted to assess the perturbation of the geo-referenced wind ~~vector~~ velocity

798 and turbulent flux under variation ($+30\%$) of each calibrat~~ioned~~ parameter around its ~~calibrated~~ optimum value ($\epsilon_\psi =$

799 $2°, \epsilon_\theta =- 0.183°, \epsilon_\phi = 0°, \epsilon_r = 0.82$) as well as under simultaneous variation ($+30\%$) of all calibrat~~ioned~~ parameters.

800 Their RE was used to evaluate the sensitivity, and values of wind and flux less than their least resolvable magnitude were

801 removed from the calculation. ~~The sensitivity analysis was carried out based on the straight flight leg (about 4 km) by adding~~

802 ~~an error of ±30 % to the calibrated parameter value and then calculating the RE of the geo-referenced wind vector and~~

803 ~~turbulent flux between the calibrated and added error sets of results. Values less than the least resolvable magnitude were~~

804 ~~removed from the dataset.~~ The results revealed that uncertainties in the temperature recovery factor (ϵ_r) and mounting offset

805 in roll angle (ϵ_φ) do not significantly contribute to an error in the measurement of wind vector and turbulent fluxes. The

806 typical RE for the geo-referenced wind measurements is less than 1.2 % with variance less than 3 %, and the typical RE for

807 turbulent flux is less than 1.1 % with variance less than 5 %. ~~The sign of the added errors of ϵ_φ and ϵ_r also has no significant~~

808 ~~effect on the sign of the RE.~~ Calibration parameters that had the largest effect on the measurement of geo-referenced wind

809 vector and turbulent flux are the mounting offset angle in pitch (ϵ_θ) and heading (ϵ_ψ). Uncertainties in ϵ_θ had a direct effect

810 on the measurement of vertical wind component, and ~~these~~ then these errors propagate to the measured fluxes, resulting in a

811 large ~~fluctuation~~ error contains in the ~~RE (~12 %)~~measured fluxes (~15 %). A negative error ~~of~~ in the ϵ_θ will ~~resulted~~

812 ~~in~~lead to ~~smaller~~ an underestimation of the vertical wind and vice versa. ~~Uncertainties~~ Errors in ϵ_ψ directly affect the

813 measurement of the horizontal wind, and to some extent, the measurement of turbulent flux. The ~~most obvious~~

814 ~~phenomenon~~difference is that the added error in ϵ_ψ lead to a great variability (up to 25 %) in the RE of horizontal wind. By

815 checking the relationship between the magnitude of the horizontal wind (u, v) and RE, a near exponential relationships was

816 seen, as shown in Figure 10. ~~As shown in Figure 7, t~~The influence of the error in the ϵ_ψ decreased significantly with the

817 increase in the magnitude of the horizontal wind velocity. Additionally, the measurement of latent heat flux may be greatly

818 affected by the error in ε_ψ, which is reflected by the relatively large deviancy ($\sim$14 %) of the *RE*. Therefore, calibration
819 parameter ε_θ and ε_ψ need to be carefully calibrated.
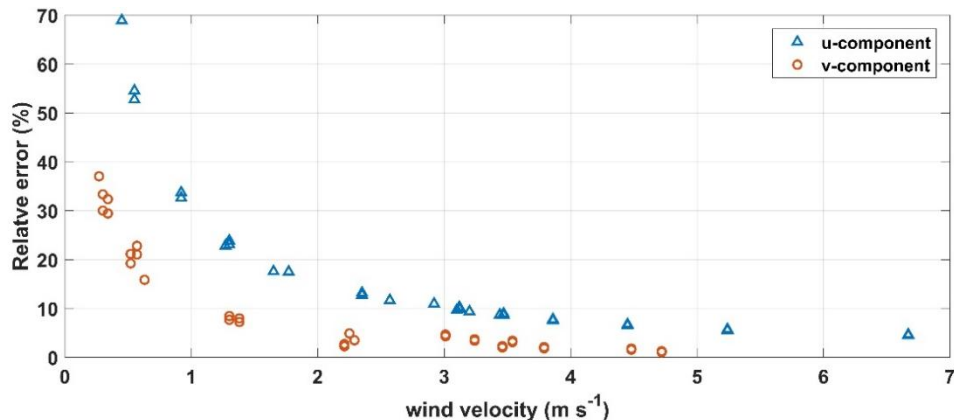
820

821 **Figure 107. Relationship between the magnitude of the horizontal wind velocity (u, v) and *RE* from the sensitivity test. ~~Wind~~**
822 ~~**velocity of less than 0.2 m s⁻¹ was excluded.**~~

823 ~~The second sensitivity test varied all the external calibration parameters simultaneously, which resulted in a slightly larger~~
824 ~~but similarly varied *RE*s compared with the first test. The results confirm that the quality of calibration parameter ε_θ and ε_ψ~~
825 ~~had the largest effect on the reliability of measurement for geo-referenced wind vector and turbulent flux. The parameter ε_θ~~
826 ~~directly affected the measurement of vertical wind and propagated its errors to the measured turbulent flux. The parameter ε_ψ~~
827 ~~significantly affected the measurement of horizontal wind, and in the measurement of turbulent flux, its effect on latent heat~~
828 ~~flux was somewhat more pronounced than for other fluxes. Therefore, these two parameters need to be carefully calibrated.~~

829 Lastly, it should be noted that the accuracy of the measured geo-referenced wind vector and turbulent flux from the UAV-
830 based EC system is subject to the combination of many factors, mainly including sensor accuracy, UAV powerplant, UAV
831 fluctuation (e.g., variation of the UAV attitude and flight height), and the atmospheric conditions during the measurements,
832 etc. This study mainly focused on assessing the effects of sensor precision and UAV powerplant on the measurement errors
833 of geo-referenced wind vector and turbulent flux. Evaluation results gave the lowest limit of the wind vector and turbulent
834 flux that the UAV-based EC system can measure. ~~this study could not evaluate the accuracy of the measured geo-referenced~~
835 ~~wind vector and turbulent flux by the UAV-based EC system compared to their actual true value. An~~Another effective way
836 to evaluate the measurement accuracy of this new technique is by comparing measured values with those from the
837 traditionally recognized measurement. However, the direct comparison of flux measurements between aircraft and traditional
838 ground tower is still challenging due to the difference in the measurement height, mechanism (time series for ground EC and
839 space series for aircraft), and instruments (e.g., wind sensor). Previous studies have extensively compared the measurement
840 of fluxes and wind vector between airborne and ground-based EC methods and found consistent results (Gioli et al., 2004;
841 Metzger et al., 2012; Sun et al., 2021b). At the same time, substantial and consistent over- or underestimation of the
842 measured wind and fluxes by UAV compared to ground measurements were observed and reported. These differences may

843 be due to several factors such as vertical flux divergence (the measurement height of UAV is higher than ground-tower),
844 surface heterogeneity (induced by the larger footprint region of the UAV compared to the ground tower), measurement
845 errors (e.g., window length, resonance noise, etc.) as well as their difference in platform and sensors. Therefore, it is
846 necessary to conduct a comparison test on the same platform and under the same environment to exclude the influence of
847 these factors. Inspired by Reineman et al. (2013), future work can include developing a ground-vehicle-based UAV flux
848 validation platform. This platform could carry both the UAV-based and traditional ground EC system to assess the
849 measurement accuracy of the UAV-based EC system with the measurement of ground EC as the benchmark in a flight-like
850 scenario.

5 Conclusions and further works

852 The main objective of this study was to quantitatively evaluate the performance of the developed UAV-based EC system in
853 the measurement of geo-referenced wind vector and turbulent flux. In terms of measuring precision, turbulence
854 measurements from the UAV-based EC system were achieved with sufficient precision to enable reliable measurement of
855 geo-referenced wind and EC flux. Magnitudes larger than 0.~~2~~ 7 m s^{-1} for wind velocity, 0.~~4~~ 3 μmol m^{-2} s^{-1} for CO_2 flux,
856 ~~80.~~0.52 W m^{-2} for sensible heat flux, and 0.8 W m^{-2} for ~~and~~ latent heat flux~~, and 0.1 m s^{-1} for friction velocity~~ could be
857 reliably measured by the UAV-based EC system by assuming the minimum required signal-to-noise ratio of 10~~5~~:1 for EC
858 application. Based on the data from the calibration flight, the carefully calibrated offset angle in pitch (ϵ_θ) and heading (ϵ_ψ)
859 were shown to effectively improve the quality of wind field measurements, and the influences of flow distortion and the
860 leverage effect on the wind measurement were minimal and could be ignored. The influence of resonance noise was small on
861 the measurement of air temperature and water vapor (typically < 1 % for their variance and flux covariance), but relatively
862 large on the measurement of CO_2 (around 5 % for variance and flux covariance).
863 The relevance of the calibration parameters (ε_r, ϵ_ϕ, ε_ψ, ε_θ) for the measurement of the geo-referenced wind vector and
864 turbulent flux was also assessed based on two sensitivity tests. ~~uncertainties in the external calibration parameters~~
865 ~~(ε_r, ϵ_ϕ, ε_ψ, ε_θ) to the computation of geo-referenced wind vector and turbulent flux was also assessed based on a sensitivity~~
866 ~~test.~~ The measurements of the geo-referenced wind vector and turbulent flux were insensitive to the errors in the ε_r and ϵ_ϕ.
867 ~~The u~~Uncertainties in the calibration parameter ε_θ and ε_ψ had the strongest effects on the measurements. Because of ε_θ
868 directly ~~effects~~ determining the magnitude of the vertical wind, its error will ~~create~~ lead to ~~inaccuracies~~ uncertainties in
869 vertical wind measurement and then propagate the ~~errors~~ uncertainties to the measurement of turbulent flux. The
870 uncertainties in ε_ψ have a direct effect on the measurement of horizontal wind, and to some extent, the measurement of
871 turbulent flux. Therefore, these two calibration parameters need to be carefully calibrated. Conducting the UAV-based EC
872 measurement when wind velocity is larger than ~~1~~ 2 m s^{-1} can led to more stable and reliable (RE < 20%) results of the wind
873 speed measurement compared to a relatively windless environmental ~~(< 1 m s^{-1})~~.

Finally, we concluded that Tthe developed UAV-based EC system measured the geo-referenced wind vector and turbulent flux with sufficient precision. The lift-induced upwash and leverage effect had almost no effect on the measurement of geo-referenced wind vector. The resonance effect caused by the operation of engine and propeller mainly affected the measurement of CO_2, and its effect on variance and flux covariance was around 5 %. The quality of calibration parameters ε_ψ and ε_θ has a significant effect on the measurement of the geo-referenced wind vector and turbulent flux, underscoring the importance of careful calibration. Although UAV-based EC measurements have many advantages over manned aircraft and tower-based EC measurements, airborne EC measurements themselves have some shortcomings, such as flux results hard to interpret (e.g., influence from surface heterogeneity, flux divergence, etc.), the measurements are restricted to short periods of time, and the interaction between the UAV and turbulence. Future researches may include the development of a new generation UAV-based EC system with the following improvements: 1) a new electro-powered UAV platform with the advantages of being quieter (low noise), having a low cruising speed, and being easy to operate; 2) a ground-vehicle-based validation platform to enable direct comparative evaluation of the UAV-based EC system with traditional ground EC methods under near-identical environmental conditions; 3) a graphics based real-time monitoring system to make it possible to change the flight pattern according to real-time data; and 4) a number of integrated field observation experiments that combining ground-based EC networks, OMS, and multi-source satellite RS to further prompt the development of theory and methodology for scaling transformation. Ultimately, the versatility of the UAV-based EC system as a low cost and widely applicable environmental research aircraft facilitates further improving our understanding of the energy and matter cycling processes at regional scales.

Author contributions. SY, GB and LX planned the field campaign; SY, LB, JJ, ZZ and JS carried out the field measurements. SY and, LS and XZ analysed the data and wrote the manuscript draft. XZ, SB, and QZ reviewed and edited the manuscript.

Competing interests. The authors declare that they have no conflict of interest.

Acknowledgments. This work was supported by the National Natural Science Foundation of China (Grant No. 42101477). We would like to thank F-EYE UAV Technology Co. Ltd. for building, maintaining, and operating the UAV in this study.

Data availability. Data for this research are not publicly available due to its proprietary nature currently. The UAV calibration flight data and the standard operation flight data in this study are available upon request to the corresponding author.

References

Anderson, K. and Gaston, K. J.: Lightweight unmanned aerial vehicles will revolutionize spatial ecology, Frontiers in Ecology and the Environment, 11, 138-146, https://doi.org/10.1890/120150, 2013.

Bange, J. and Roth, R.: Helicopter-Borne Flux Measurements in the Nocturnal Boundary Layer Over Land – a Case Study, Boundary-Layer Meteorology, 92, 295-325, 10.1023/A:1002078712313, 1999.

Båserud, L., Reuder, J., Jonassen, M. O., Kral, S. T., Paskyabi, M. B., and Lothon, M.: Proof of concept for turbulence measurements with the RPAS SUMO during the BLLAST campaign, Atmos. Meas. Tech., 9, 4901-4913, 10.5194/amt-9-4901-2016, 2016.

Billesbach, D. P.: Estimating uncertainties in individual eddy covariance flux measurements: A comparison of methods and a proposed new method, Agricultural and Forest Meteorology, 151, 394-405, https://doi.org/10.1016/j.agrformet.2010.12.001, 2011.

Chandra, N., Patra, P. K., Niwa, Y., Ito, A., Iida, Y., Goto, D., Morimoto, S., Kondo, M., Takigawa, M., Hajima, T., and Watanabe, M.: Estimated regional CO_2 flux and uncertainty based on an ensemble of atmospheric CO_2 inversions, Atmos. Chem. Phys., 22, 9215-9243, 10.5194/acp-22-9215-2022, 2022.

Chen, J. M., Leblanc, S. G., Cihlar, J., Desjardins, R. L., and MacPherson, J. I.: Extending aircraft- and tower-based CO_2 flux measurements to a boreal region using a Landsat thematic mapper land cover map, Journal of Geophysical Research: Atmospheres, 104, 16859-16877, https://doi.org/10.1029/1999JD900129, 1999.

Chen, W., Wang, D., Huang, Y., Chen, L., Zhang, L., Wei, X., Sang, M., Wang, F., Liu, J., and Hu, B.: Monitoring and analysis of coastal reclamation from 1995–2015 in Tianjin Binhai New Area, China, Scientific Reports, 7, 3850, 10.1038/s41598-017-04155-0, 2017.

Crawford, T. L. and Dobosy, R. J.: A sensitive fast-response probe to measure turbulence and heat flux from any airplane, Boundary-Layer Meteorology, 59, 257-278, 10.1007/BF00119816, 1992.

Crawford, T. L., Dobosy, R. J., and Dumas, E. J.: Aircraft wind measurement considering lift-induced upwash, Boundary-Layer Meteorology, 80, 79-94, 10.1007/BF00119012, 1996.

Desjardins, R. L., Brach, E. J., Alvo, P., and Schuepp, P. H.: Aircraft Monitoring of Surface Carbon Dioxide Exchange, Science, 216, 733-735, 10.1126/science.216.4547.733, 1982.

Desjardins, R. L., Worth, D. E., MacPherson, J. I., Bastian, M., and Srinivasan, R.: Flux measurements by the NRC Twin Otter atmospheric research aircraft: 1987–2011, Adv. Sci. Res., 13, 43-49, 10.5194/asr-13-43-2016, 2016.

Drüe, C. and Heinemann, G.: A Review and Practical Guide to In-Flight Calibration for Aircraft Turbulence Sensors, Journal of Atmospheric and Oceanic Technology, 30, 2820-2837, 10.1175/JTECH-D-12-00103.1, 2013.

Elston, J., Argrow, B., Stachura, M., Weibel, D., Lawrence, D., and Pope, D.: Overview of Small Fixed-Wing Unmanned Aircraft for Meteorological Sampling, Journal of Atmospheric and Oceanic Technology, 32, 97-115, 10.1175/JTECH-D-13-00236.1, 2015.

935 Enriquez, A. G. and Friehe, C. A.: Effects of Wind Stress and Wind Stress Curl Variability on Coastal Upwelling, Journal of
936 Physical Oceanography, 25, 1651-1671, https://doi.org/10.1175/1520-0485(1995)025<1651:EOWSAW>2.0.CO;2, 1995.

937 Finkelstein, P. L. and Sims, P. F.: Sampling error in eddy correlation flux measurements, Journal of Geophysical Research:
938 Atmospheres, 106, 3503-3509, https://doi.org/10.1029/2000JD900731, 2001.

939 Garman, K. E., Wyss, P., Carlsen, M., Zimmerman, J. R., Stirm, B. H., Carney, T. Q., Santini, R., and Shepson, P. B.: The
940 Contribution of Variability of Lift-induced Upwash to the Uncertainty in Vertical Winds Determined from an Aircraft
941 Platform, Boundary-Layer Meteorology, 126, 461-476, 10.1007/s10546-007-9237-y, 2008.

942 Garman, K. E., Hill, K. A., Wyss, P., Carlsen, M., Zimmerman, J. R., Stirm, B. H., Carney, T. Q., Santini, R., and Shepson,
943 P. B.: An Airborne and Wind Tunnel Evaluation of a Wind Turbulence Measurement System for Aircraft-Based Flux
944 Measurements, Journal of Atmospheric and Oceanic Technology, 23, 1696-1708, 10.1175/JTECH1940.1, 2006.

945 Gioli, B., Miglietta, F., Vaccari, F. P., and Zaldei, A.: The Sky Arrow ERA, an innovative airborne platform to monitor mass,
946 momentum and energy exchange of ecosystems, Annals of Geophysics, 49, 109-116, 10.4401/ag-3159, 2006.

947 Gioli, B., Miglietta, F., De Martino, B., Hutjes, R. W. A., Dolman, H. A. J., Lindroth, A., Schumacher, M., Sanz, M. J.,
948 Manca, G., Peressotti, A., and Dumas, E. J.: Comparison between tower and aircraft-based eddy covariance fluxes in five
949 European regions, Agricultural and Forest Meteorology, 127, 1-16, https://doi.org/10.1016/j.agrformet.2004.08.004, 2004.

950 Hannun, R. A., Wolfe, G. M., Kawa, S. R., Hanisco, T. F., Newman, P. A., Alfieri, J. G., Barrick, J., Clark, K. L., DiGangi, J.
951 P., Diskin, G. S., King, J., Kustas, W. P., Mitra, B., Noormets, A., Nowak, J. B., Thornhill, K. L., and Vargas, R.: Spatial
952 heterogeneity in CO2, CH4, and energy fluxes: insights from airborne eddy covariance measurements over the Mid-Atlantic
953 region, Environmental Research Letters, 15, 035008, 10.1088/1748-9326/ab7391, 2020.

954 Hu, G. and Jia, L.: Monitoring of Evapotranspiration in a Semi-Arid Inland River Basin by Combining Microwave and
955 Optical Remote Sensing Observations, Remote Sensing, 7, 10.3390/rs70303056, 2015.

956 Kaimal, J. C., Clifford, S. F., and Lataitis, R. J.: Effect of finite sampling on atmospheric spectra, Boundary-Layer
957 Meteorology, 47, 337-347, 10.1007/BF00122338, 1989.

958 Kalogiros, J. A. and Wang, Q.: Aerodynamic Effects on Wind Turbulence Measurements with Research Aircraft, Journal of
959 Atmospheric and Oceanic Technology, 19, 1567-1576, 10.1175/1520-0426(2002)019<1567:AEOWTM>2.0.CO;2, 2002.

960 Khelif, D., Burns, S. P., and Friehe, C. A.: Improved Wind Measurements on Research Aircraft, Journal of Atmospheric and
961 Oceanic Technology, 16, 860-875, 10.1175/1520-0426(1999)016<0860:IWMORA>2.0.CO;2, 1999.

962 Kirby, S., Dobosy, R., Williamson, D., and Dumas, E.: An aircraft-based data analysis method for discerning individual
963 fluxes in a heterogeneous agricultural landscape, Agricultural and Forest Meteorology, 148, 481-489,
964 https://doi.org/10.1016/j.agrformet.2007.10.011, 2008.

965 Kowalski, A. S., Serrano-Ortiz, P., Miranda-García, G., and Fratini, G.: Disentangling Turbulent Gas Diffusion from Non-
966 diffusive Transport in the Boundary Layer, Boundary-Layer Meteorology, 179, 347-367, 10.1007/s10546-021-00605-5,
967 2021.

Lenschow, D. H.: Aircraft Measurements in the Boundary Layer, in: Probing the Atmospheric Boundary Layer, edited by: Lenschow, D. H., American Meteorological Society, Boston, MA, Boston, https://doi.org/10.1007/978-1-944970-14-7_5, 1986.

Lenschow, D. H. and Sun, J.: The spectral composition of fluxes and variances over land and sea out to the mesoscale, Boundary-Layer Meteorology, 125, 63-84, 10.1007/s10546-007-9191-8, 2007.

Lenschow, D. H., Delany, A. C., Stankov, B. B., and Stedman, D. H.: Airborne measurements of the vertical flux of ozone in the boundary layer, Boundary-Layer Meteorology, 19, 249-265, 10.1007/BF00117223, 1980.

Li, X., Liu, S., Xiao, Q., Ma, M., Jin, R., Che, T., Wang, W., Hu, X., Xu, Z., Wen, J., and Wang, L.: A multiscale dataset for understanding complex eco-hydrological processes in a heterogeneous oasis system, Scientific Data, 4, 170083, 10.1038/sdata.2017.83, 2017.

Li, X., Liu, S., Yang, X., Ma, Y., He, X., Xu, Z., Xu, T., Song, L., Zhang, Y., Hu, X., Ju, Q., and Zhang, X.: Upscaling Evapotranspiration from a Single-Site to Satellite Pixel Scale, 10.3390/rs13204072, 2021.

Li, X., Liu, S., Li, H., Ma, Y., Wang, J., Zhang, Y., Xu, Z., Xu, T., Song, L., Yang, X., Lu, Z., Wang, Z., and Guo, Z.: Intercomparison of Six Upscaling Evapotranspiration Methods: From Site to the Satellite Pixel, Journal of Geophysical Research: Atmospheres, 123, 6777-6803, https://doi.org/10.1029/2018JD028422, 2018.

Liu, H., Randerson, J. T., Lindfors, J., Massman, W. J., and Foken, T.: Consequences of Incomplete Surface Energy Balance Closure for CO2 Fluxes from Open-Path CO2/H2O Infrared Gas Analysers, Boundary-Layer Meteorology, 120, 65-85, 10.1007/s10546-005-9047-z, 2006.

Liu, J., Chen, J. M., Cihlar, J., and Chen, W.: Net primary productivity distribution in the BOREAS region from a process model using satellite and surface data, Journal of Geophysical Research: Atmospheres, 104, 27735-27754, https://doi.org/10.1029/1999JD900768, 1999.

Liu, S., Xu, Z., Song, L., Zhao, Q., Ge, Y., Xu, T., Ma, Y., Zhu, Z., Jia, Z., and Zhang, F.: Upscaling evapotranspiration measurements from multi-site to the satellite pixel scale over heterogeneous land surfaces, Agricultural and Forest Meteorology, 230-231, 97-113, https://doi.org/10.1016/j.agrformet.2016.04.008, 2016.

Liu, S., Li, X., Xu, Z., Che, T., Xiao, Q., Ma, M., Liu, Q., Jin, R., Guo, J., Wang, L., Wang, W., Qi, Y., Li, H., Xu, T., Ran, Y., Hu, X., Shi, S., Zhu, Z., Tan, J., Zhang, Y., and Ren, Z.: The Heihe Integrated Observatory Network: A Basin-Scale Land Surface Processes Observatory in China, Vadose Zone Journal, 17, 180072, https://doi.org/10.2136/vzj2018.04.0072, 2018.

Mahrt, L.: Flux Sampling Errors for Aircraft and Towers, Journal of Atmospheric and Oceanic Technology, 15, 416-429, https://doi.org/10.1175/1520-0426(1998)015<0416:FSEFAA>2.0.CO;2, 1998.

Massman, W. and Clement, R.: Uncertainty in Eddy Covariance Flux Estimates Resulting from Spectral Attenuation, in: Handbook of Micrometeorology: A Guide for Surface Flux Measurement and Analysis, edited by: Lee, X., Massman, W., and Law, B., Springer Netherlands, Dordrecht, 67-99, 10.1007/1-4020-2265-4_4, 2005.

1001   Mathez, E. and Smerdon, J.: Climate Change3. Ocean– Atmosphere Interactions, in: The Science of Global Warming and
1002   Our Energy Future, Columbia University Press, 69-100, doi:10.7312/math17282-005, 2018.

1003   Mauder, M., Cuntz, M., Drüe, C., Graf, A., Rebmann, C., Schmid, H. P., Schmidt, M., and Steinbrecher, R.: A strategy for
1004   quality and uncertainty assessment of long-term eddy-covariance measurements, Agricultural and Forest Meteorology, 169,
1005   122-135, https://doi.org/10.1016/j.agrformet.2012.09.006, 2013.

1006   Mayer, J., Mayer, M., Haimberger, L., and Liu, C.: Comparison of Surface Energy Fluxes from Global to Local Scale,
1007   Journal of Climate, 35, 4551-4569, 10.1175/JCLI-D-21-0598.1, 2022.

1008   Metzger, S., Junkermann, W., Butterbach-Bahl, K., Schmid, H. P., and Foken, T.: Measuring the 3-D wind vector with a
1009   weight-shift microlight aircraft, Atmos. Meas. Tech., 4, 1421-1444, 10.5194/amt-4-1421-2011, 2011.

1010   Metzger, S., Junkermann, W., Mauder, M., Beyrich, F., Butterbach-Bahl, K., Schmid, H. P., and Foken, T.: Eddy-covariance
1011   flux measurements with a weight-shift microlight aircraft, Atmos. Meas. Tech., 5, 1699-1717, 10.5194/amt-5-1699-2012,
1012   2012.

1013   Mohan, M. M. P., Rajitha, K., and Murari, R. R. V.: Review of approaches for the estimation of sensible heat flux in remote
1014   sensing-based evapotranspiration models, Journal of Applied Remote Sensing, 14, 1-31, 10.1117/1.JRS.14.041501, 2020.

1015   Peltola, O., Aslan, T., Ibrom, A., Nemitz, E., Rannik, Ü., and Mammarella, I.: The high-frequency response correction of
1016   eddy covariance fluxes – Part 1: An experimental approach and its interdependence with the time-lag estimation, Atmos.
1017   Meas. Tech., 14, 5071-5088, 10.5194/amt-14-5071-2021, 2021.

1018   Prudden, S., Fisher, A., Marino, M., Mohamed, A., Watkins, S., and Wild, G.: Measuring wind with Small Unmanned
1019   Aircraft Systems, Journal of Wind Engineering and Industrial Aerodynamics, 176, 197-210,
1020   https://doi.org/10.1016/j.jweia.2018.03.029, 2018.

1021   Prueger, J. H., Hatfield, J. L., Parkin, T. B., Kustas, W. P., Hipps, L. E., Neale, C. M. U., MacPherson, J. I., Eichinger, W. E.,
1022   and Cooper, D. I.: Tower and Aircraft Eddy Covariance Measurements of Water Vapor, Energy, and Carbon Dioxide Fluxes
1023   during SMACEX, Journal of Hydrometeorology, 6, 954-960, 10.1175/JHM457.1, 2005.

1024   Rannik, Ü., Peltola, O., and Mammarella, I.: Random uncertainties of flux measurements by the eddy covariance technique,
1025   Atmos. Meas. Tech., 9, 5163-5181, 10.5194/amt-9-5163-2016, 2016.

1026   Reineman, B. D., Lenain, L., Statom, N. M., and Melville, W. K.: Development and Testing of Instrumentation for UAV-
1027   Based Flux Measurements within Terrestrial and Marine Atmospheric Boundary Layers, Journal of Atmospheric and
1028   Oceanic Technology, 30, 1295-1319, 10.1175/JTECH-D-12-00176.1, 2013.

1029   Reuder, J., Båserud, L., Jonassen, M. O., Kral, S. T., and Müller, M.: Exploring the potential of the RPA system SUMO for
1030   multipurpose boundary-layer missions during the BLLAST campaign, Atmos. Meas. Tech., 9, 2675-2688, 10.5194/amt-9-
1031   2675-2016, 2016.

1032   Sayres, D. S., Dobosy, R., Healy, C., Dumas, E., Kochendorfer, J., Munster, J., Wilkerson, J., Baker, B., and Anderson, J. G.:
1033   Arctic regional methane fluxes by ecotope as derived using eddy covariance from a low-flying aircraft, Atmos. Chem. Phys.,
1034   17, 8619-8633, 10.5194/acp-17-8619-2017, 2017.

1035 Serrano-Ortiz, P., Kowalski, A. S., Domingo, F., Ruiz, B., and Alados-Arboledas, L.: Consequences of Uncertainties in CO_2
1036 Density for Estimating Net Ecosystem CO_2 Exchange by Open-path Eddy Covariance, Boundary-Layer Meteorology, 126,
1037 209-218, 10.1007/s10546-007-9234-1, 2008.

1038 Sun, Y., Jia, L., Chen, Q., and Zheng, C.: Optimizing Window Length for Turbulent Heat Flux Calculations from Airborne
1039 Eddy Covariance Measurements under Near Neutral to Unstable Atmospheric Stability Conditions, Remote Sensing, 10,
1040 10.3390/rs10050670, 2018.

1041 Sun, Y., Ma, J., Sude, B., Lin, X., Shang, H., Geng, B., Diao, Z., Du, J., and Quan, Z.: A UAV-Based Eddy Covariance
1042 System for Measurement of Mass and Energy Exchange of the Ecosystem: Preliminary Results, Sensors, 21,
1043 10.3390/s21020403, 2021a.

1044 Sun, Y., Sude, B., Geng, B., Ma, J., Lin, X., Hao, Z., Jing, W., Chen, Q., and Quan, Z.: Observation of the winter regional
1045 evaporative fraction using a UAV-based eddy covariance system over wetland area, Agricultural and Forest Meteorology,
1046 310, 108619, https://doi.org/10.1016/j.agrformet.2021.108619, 2021b.

1047 Thomas, R. M., Lehmann, K., Nguyen, H., Jackson, D. L., Wolfe, D., and Ramanathan, V.: Measurement of turbulent water
1048 vapor fluxes using a lightweight unmanned aerial vehicle system, Atmos. Meas. Tech., 5, 243-257, 10.5194/amt-5-243-2012,
1049 2012.

1050 van den Kroonenberg, A., Martin, T., Buschmann, M., Bange, J., and Vörsmann, P.: Measuring the Wind Vector Using the
1051 Autonomous Mini Aerial Vehicle M2AV, Journal of Atmospheric and Oceanic Technology, 25, 1969-1982,
1052 10.1175/2008JTECHA1114.1, 2008.

1053 van den Kroonenberg, A. C., Martin, S., Beyrich, F., and Bange, J.: Spatially-Averaged Temperature Structure Parameter
1054 Over a Heterogeneous Surface Measured by an Unmanned Aerial Vehicle, Boundary-Layer Meteorology, 142, 55-77,
1055 10.1007/s10546-011-9662-9, 2012.

1056 Vellinga, O. S., Dobosy, R. J., Dumas, E. J., Gioli, B., Elbers, J. A., and Hutjes, R. W. A.: Calibration and Quality Assurance
1057 of Flux Observations from a Small Research Aircraft*, Journal of Atmospheric and Oceanic Technology, 30, 161-181,
1058 10.1175/JTECH-D-11-00138.1, 2013.

1059 Vellinga, O. S., Gioli, B., Elbers, J. A., Holtslag, A. A. M., Kabat, P., and Hutjes, R. W. A.: Regional carbon dioxide and
1060 energy fluxes from airborne observations using flight-path segmentation based on landscape characteristics, Biogeosciences,
1061 7, 1307-1321, 10.5194/bg-7-1307-2010, 2010.

1062 Wang, H., Jia, G., Zhang, A., and Miao, C.: Assessment of Spatial Representativeness of Eddy Covariance Flux Data from
1063 Flux Tower to Regional Grid, Remote Sensing, 8, 742, 2016.

1064 Webb, E. K., Pearman, G. I., and Leuning, R.: Correction of flux measurements for density effects due to heat and water
1065 vapour transfer, Quarterly Journal of the Royal Meteorological Society, 106, 85-100,
1066 https://doi.org/10.1002/qj.49710644707, 1980.

1067 Williams, A. and Marcotte, D.: Wind Measurements on a Maneuvering Twin-Engine Turboprop Aircraft Accounting for
1068 Flow Distortion, Journal of Atmospheric and Oceanic Technology, 17, 795-810, 10.1175/1520-
1069 0426(2000)017<0795:WMOAMT>2.0.CO;2, 2000.

1070 Witte, B. M., Singler, R. F., and Bailey, S. C. C.: Development of an Unmanned Aerial Vehicle for the Measurement of
1071 Turbulence in the Atmospheric Boundary Layer, Atmosphere, 8, 10.3390/atmos8100195, 2017.

1072 Wolfe, G. M., Kawa, S. R., Hanisco, T. F., Hannun, R. A., Newman, P. A., Swanson, A., Bailey, S., Barrick, J., Thornhill, K.
1073 L., Diskin, G., DiGangi, J., Nowak, J. B., Sorenson, C., Bland, G., Yungel, J. K., and Swenson, C. A.: The NASA Carbon
1074 Airborne Flux Experiment (CARAFE): instrumentation and methodology, Atmos. Meas. Tech., 11, 1757-1776,
1075 10.5194/amt-11-1757-2018, 2018.

1076 Xu, S., Xu, S., Zhou, Y., Yue, S., Zhang, X., Gu, R., Zhang, Y., Qiao, Y., and Liu, M.: Long-Term Changes in the Unique
1077 and Largest Seagrass Meadows in the Bohai Sea (China) Using Satellite (1974–2019) and Sonar Data: Implication for
1078 Conservation and Restoration, Remote Sensing, 13, 856, 10.3390/rs13050856, 2021.

1079 Yang, X., Yong, B., Ren, L., Zhang, Y., and Long, D.: Multi-scale validation of GLEAM evapotranspiration products over
1080 China via ChinaFLUX ET measurements, International Journal of Remote Sensing, 38, 5688-5709,
1081 10.1080/01431161.2017.1346400, 2017.

1082 Zhang, G., Zhang, J., and Meng, P.: Estimation of kilometer-scale heat fluxes over a hilly area in Northern China using an
1083 optical-microwave scintillometer, Agricultural Water Management, 244, 106582,
1084 https://doi.org/10.1016/j.agwat.2020.106582, 2021.

1085 Zheng, C., Liu, S., Song, L., Xu, Z., Guo, J., Ma, Y., Ju, Q., and Wang, J.: Comparison of sensible and latent heat fluxes
1086 from optical-microwave scintillometers and eddy covariance systems with respect to surface energy balance closure,
1087 Agricultural and Forest Meteorology, 331, 109345, https://doi.org/10.1016/j.agrformet.2023.109345, 2023.

1088